ON PREDICTING THE THRESHOLD CURRENT DENSITY OF QUANTUM WELL DIODE LASERS

By

GABGYU LIM

A DISSERTATION PRESENTED TO THE GRADUATE SCHOOL
OF THE UNIVERSITY OF FLORIDA
IN PARTIAL FULFILLMENT OF THE REQUIREMENTS
FOR THE DEGREE OF DOCTOR OF PHILOSOPHY

UNIVERSITY OF FLORIDA
1992

UNIVERSITY OF FLORIDA LIBRARIES

TO THE GLORY OF MY GOD
AND
IN MEMORY OF MY MOTHER, HAKYI NAM (1907-1990)

ACKNOWLEDGEMENTS

I wish to express my sincere gratitude to my advisor, Professor Peter S. Zory, for his guidance, encouragement and for his financial support. I thank Professors Sheng S. Li, Ramakant Srivastava, Gijs Bosman, and Timothy Anderson for serving on my supervisory committee.

I also thank Dr. Luis Figueroa of the Boeing Aerospace & Electronics High Technology Center who motivated my interest in semiconductor lasers and who had been my advisor for two years. I am very grateful to Dr. Charles A. Zmudzinski for his valuable help on the experiment. I would like to thank Mr. Youngsoh Park for processing and packaging the materials and Dr. Hsing-Chien Cheng for his help on software. My appreciation is also extended to the members of the Photonics Research Laboratory, especially Dr. Yu Guan, Mr. Douglas Hudson, Mr. Christopher Fuligni, and Mr. Horngiye Luo for their support and friendship.

I am grateful to my brothers for their encouragement and support. Finally, I would like to thank to my wife, Taehee, and lovely daughters, Sulgi and Hyanggi, for their hardships, support, love, and prayers during my study.

This work was supported in part by the Boeing Aerospace & Electronics High Technology Center.

TABLE OF CONTENTS

Page
ACKNOWLEDGEMENTS....iii
ABSTRACT....vi
CHAPTER
1. INTRODUCTION....1
2. COMPARISON OF EXPERIMENTAL J_{th}, T_o WITH CALCULATED J_{th}, T_o 7
2.1. Laser Material....7
2.2. Modal Property....9
2.3. Measurement....13
2.4. Prediction of J_{th} and T_o....13
2.5. Results and Discussions....24
2.6. Suggestion....31
3. FITTING THICK QW DATA WITH STANDARD BULK THEORY....32
3.1. Introduction....32
3.2. Predictions....33
3.3. Results and Discussions....38
3.4. Summary....45
APPENDIX A....46
4. FITTING THIN QW EXPERIMENTAL DATA WITH VBM QW THEORY....49
4.1. Introduction....49
4.2. Valence Band Mixing Quantum Well Theory....50

4.2.1. Effective Mass Equations....................50
4.2.2. Transition Matrix Element....................58
4.2.3. Expression for Gain and Spontaneous Emission....................59
4.2.3.1. Gain....................59
4.2.3.2. Spontaneous Emission....................60
4.2.3.3. Carrier Density and Quasi-Fermi Level....................62
4.3. Numerical Results and Discussions....................63
4.4. Summary....................80

5. SUMMARY AND CONCLUSIONS....................85

REFERENCES....................88

BIOGRAPHICAL SKETCH....................93

Abstract of Dissertation Presented to the Graduate School
of the University of Florida in Partial Fulfillment of the
Requirements for the Degree of Doctor of Philosophy

ON PREDICTING THE THRESHOLD CURRENT DENSITY OF QUANTUM WELL DIODE LASERS

By
Gabgyu Lim
May, 1992

Chairman: Peter S. Zory
Major Department: Electrical Engineering

The threshold current density of GaAs/AlGaAs graded refractive index (GRIN), separate confinement heterostructure (SCH), single quantum well (SQW) laser diodes was measured at 25°C and compared with predicted J_{th} using published CZR (Chinn, Zory, Reisinger) model. The results indicated that the existing CZR model for QW lasers was found to be deficient.

To sort out the problem, we chose two cases, thick 40nm well (bulk) and thin 7.5 nm QW. In thick wells, all the complicated phenomena related to the QW vanish and only carrier scattering (CS) is expected to be fundamental. We investigated the effect of CS on J_{th} using standard bulk theory. In thin 7.5 nm QW where quantum size and nonradiative effects are important, we studied the effect of CS on J_{th} using new valence band mixing (VBM) QW theory.

A reasonable fit to the thick QW(bulk) experimental data at both 25°C and 125°C could be obtained using strict k-selection bulk theory and a knowledge of the carrier injection efficiency(η_{in}). In making the fit, CS effect is not necessary, quite contrary to Yamada's results. This finding suggested the possibility that the effect of CS on J_{th} might not be important even in thin QW lasers. This was verified with VBM QW theory combined with a knowledge of the carrier injection efficiency(η_{in}). Combination of the effects by valence band mixing and measured injection efficiency fit the 7.5 nm QW experimental data, leaving no room for the CS contribution. Leakage current density estimated in terms of measured injection efficiency (η_{in}) is significant, comparable to the current density contribution by CS in the CZR model. This does not necessarily rule out the possibility that experimental spectra can, in principle, be obtained which are subject to the strict k-selection rule.

It is concluded that good predictions of threshold current density at any temperature can be made for QW lasers provided one uses QW theory developed in this work and one knows how to predict the temperature dependence of η_{in}.

CHAPTER 1
INTRODUCTION

The idealized light output power versus injection current relationship for semiconductor lasers is a straight line as shown in Fig. 1-1. For high performance, the threshold current (I_{th}) should be small and slope efficiency of the line big. It is well known that the quantum well (QW) design, characterized by a very thin active layer, is best for high performance.

Various aerospace applications have been envisoned in which high performance QW diode lasers are the key elements. However, many of these applications require that the devices operate reliably at temperatures as high as 125°C. QW lasers can perform better than thick active layer double heterostructure lasers at high temperature, but predicting their performance is much more complicated than predicting that for DH lasers because of their complex internal structure. The goal of this study was to integrate the results of experimental and theoretical work to determine a model capable of predicting threshold current density (J_{th}) at any temperature for QW lasers.

Many publications have been devoted to theoretical gain vs threshold current calculations through the years. The Stern model [Ster73] was largely accepted as the correct model for such calculations in the '70s, although it predicted J_{th} values not precisely

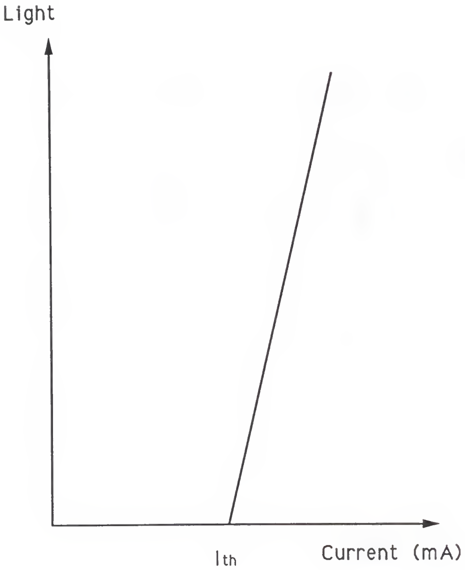

Fig. 1-1. Idealized light/current characteristic of a semiconductor laser showing threshold current I_{th} and linear slope.

the same as those measured by the best lasers of that time [Thom80]. In the early '80s, Yamada pointed out that Stern's spectral gain function was too optimistic because it ignored carrier scattering (CS). By convolving the spectral gain function with a Lorentzian broadening function (CS time of about 10^{-13} sec), Yamada and Ishiguro were able to fit their threshold data for DH lasers [Yama81]. Since then, most J_{th} modeling work for both DH and QW lasers have incorporated the CS concept [Asada84].

The above modelling works have been based on the parabolic model, which assumes a simple parabolic band for both conduction and valence band structures and a constant optical matrix element for the transitions anywhere in the bands. More recently, Chinn, Zory and Reisinger published a detailed parabolic model(≅ CZR model) [Chin88, Chin89], where valence band nonparabolicity was included for the light hole states. Other important features included in this model were intraband scattering, gain anisotropy, nonradiative processes such as leakage of the carriers over the confining potential barriers [Case78, Dutt81], and Auger recombination [Take85].

One success of the CZR model was to explain, semi-quantitatively, the anomalous temperature behaviour of J_{th} for GaAs, thin QW diode lasers observed by Zory et al. [Zory86a]. It was also used to predict J_{th} and its temperature dependence (specified by characteristic temperature T_o) for 30/70 GaAs/AlGaAs graded refractive index (GRIN), separate confinement heterostructure (SCH), single quantum well (SQW) lasers near room temperature [Chin89]. In order to verify the validity of the CZR model over a wide range of active layer thickness for 30/70 GaAs/AlGaAs GRIN- SCH-SQW laser diodes, we compared experimental J_{th} and T_0 values with the above predictions. The results showed that the CZR model can predict J_{th} reasonably well for some cases. However, it underestimates J_{th} in thin QW lasers, and overestimates J_{th} substantially for thick QW lasers. The trend of T_0 values agrees pretty well with experimental values but they are overestimated because J_{th} is not predicted properly. The possible reasons why the CZR model predictions do not agree with experiment are as follows: (i) CZR model breaks down for thick well (bulk). (ii) Lineshape function used, which was assumed to be independent of well thickness, temperature, carrier energy and carrier density, is not appropriate. (iii) Nonradiative current might not be estimated correctly. (iv) CZR model does not treat the valence band correctly. Fundamental studies [Cola87, Ahn88] have shown that the valence band structure of quantum wells deviates significantly from that of the parabolic band due to valence band mixing (VBM) as the QW width decreases. VBM gives nonparabolic bands which affect both the subband energies and the density of states functions. The density of states functions are found to differ considerably from the simple step-like shape computed from the band edge effective masses. The band mixing also results in large differences in the momentum vector dependence of the matrix elements, and moreover, some of the transitions which were previously assumed to be forbidden become partially allowed. The quantum well gain calculated by the k.p method and k-selection rules is considerably different than those from the conventional methods with parabolic bands and with matrix elements which have constant total magnitude. Although the effects of the band-mixing on the band structure and gain of a QW have been studied [Cola87, Ahn88, Zory92], very little work has been done on the comparison of theory to the experimental data.

To sort out the problem, we chose two cases, thick 40nm well (bulk) and thin 7.5 nm QW. In thick well all the complicated phenomena related to the QW vanish and only CS is expected to be fundamental. We investigated the CS effect on J_{th} using standard bulk theory [Ster73]. In thin 7.5 nm QW where quantum size and nonradiative effects are important, we studied the effect of CS on J_{th} using valence band mixing (VBM) QW theory. In the new model, the leakage current was included into the total current in terms of spontaneous emission efficiencies (η_{sp}), which can be expressed as the product of two efficiencies, η_{in} = injection efficiency and η_r = active layer radiative efficiency [Zory91, Lim91]. Injection efficiency was estimated from the differential quantum efficiency versus laser cavity length measurements. Radiative recombination rate was calculated theoretically. To calculate the band structure and electron (or hole) wavefunctions in a quantum well, we used the multiband effective-mass theory (k.p method) [Lutti55]. For simplicity, we assumed that the conduction and valence bands are decoupled, which is in fact a good approximation for wide-band-gap semiconductors such as GaAs [Sand87]. For the conduction band, a simple isotropic parabolic band was used. For the valence band, we used a 4x4 Luttinger-Kohn Hamiltonian, the elements of which are derived based on the k.p method. The multiband effective mass equations were solved numerically using the finite-difference method.

From the above work we found that a reasonable fit to the thick QW(bulk) experimental data at both 25°C and 125°C could be obtained using strict k-selection bulk theory and a knowledge of the carrier injection efficiency(η_{in}). In making the fit, carrier scattering is not necessary, quite contrary to Yamada's results [Yama81]. This finding suggested the possibility that the effect of CS on J_{th} might not be important even in thin QW lasers. This was verified with VBM QW theory combined with a knowledge of the carrier injection efficiency(η_{in}).

The thesis is organized as follows. We start with a comparison of predicted J_{th} and T_0 with experimental data in chapter 2. In Chapter 3 we present the results of fitting thick well data. In Chapter 4 we summarize the results of fitting thin QW data. Finally, we end with summary and conclusions in chapter 5.

CHAPTER 2
COMPARISON OF EXPERIMENTAL J_{th}, T_o WITH CALCULATED J_{th}, T_o

2.1. Laser Material

The lasers material used in these experiments was separate confinement heterostructure(SCH) material with a 7.5, 20, 40 nm thick, single-quantum-well(SQW) GaAs active layer sandwiched between two AlGaAs layers with Al composition graded between 30% and 70%. The GRIN-SCH-SQW material [Tsan81] shown in Fig. 2-1 was grown in conventional metal organic chemical vapour deposition (MOCVD) vertical reactor using procedures similar to those described by Dapkus [Dapk82]. The specifics of the seven layer wafer, grown at a susceptor temperature of 750°C on an n-type GaAs substrate(Si $=10^{18}$/cc), are as follows: a 1.5-μm $Al_{0.7}Ga_{0.3}As$ n-type confining layer(Si $=10^{18}$/cc), a 0.2-μm $Al_xGa_{1-x}As$ n-type graded (x=0.7-0.3) barrier layer(Si $=10^{17}$/cc), an undoped GaAs active layer, a 0.2-μm $Al_xGa_{1-x}As$ p-type graded (x=0.3-0.7) barrier layer(Mg $=10^{17}$/cc), a 1.5-μm $Al_{0.7}Ga_{0.3}As$ p-type confining layer (Mg $=10^{18}$/cc), and a 0.2-μm GaAs Mg-doped GaAs p^+ cap layer (Mg $=10^{19}$/cc).

After growth, 150 μm conducting stripes were defined on the material using 0.15 μm-thick SiO_2. For ohmic contact, metal deposition was made. The thickness of gold layer is 2000 Å for p-side and 1500 Å for n-side. But more gold was needed for good wire

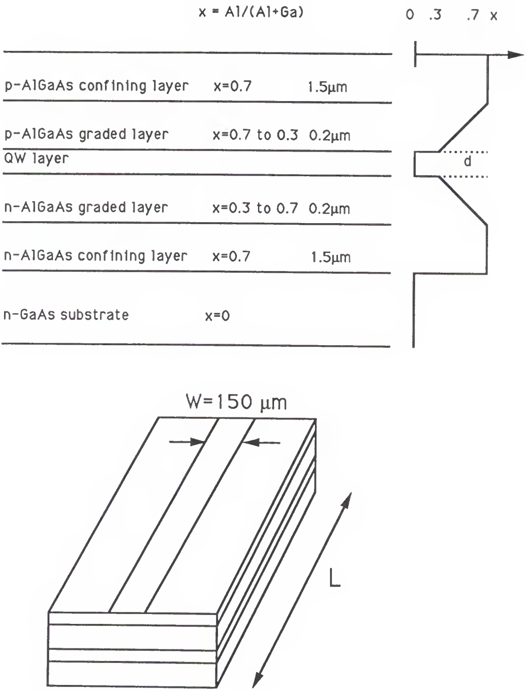
x = Al/(Al+Ga)
0 .3 .7 x
p-AlGaAs confining layer x=0.7 1.5μm
p-AlGaAs graded layer x=0.7 to 0.3 0.2μm
QW layer
d
n-AlGaAs graded layer x=0.3 to 0.7 0.2μm
n-AlGaAs confining layer x=0.7 1.5μm
n-GaAs substrate x=0
W=150 μm
L

Fig. 2-1. GRIN-SCH-SQW laser structure.

bonding on p-side, and for heat spreader on n-side. So additional gold layers of 2000 Å on p-side and 4000 Å on n-side were deposited. To make sure of good adhesion of the additional gold layer on the existing metal, 500 Å of Ti was deposited first. The deposition was done with Electron-Beam Evaporator and the pressure during the deposition was maintained at 5×10^{-6} Torr. Bars of various length were then cleaved, separated into 250, 500, 750, 1000 μm-wide chips and soldered p-side up on the copper blocks.

2.2. Modal property

Since the stimulated emission and gain coefficient are related to the photon flux, it is important to consider the field distribution in order to determine the fraction of the optical mode within the laser active layer. The extent of light coefficient within the active layer may be represented by the confinement factor Γ. Therefore Γ is defined as the ratio of the light intensity within the active layer to the sum of light intensity both within and outside the active layer, which can be given by [Bote84]

$$\Gamma = \frac{\int_{-d/2}^{d/2} |E_y|^2 \, dz}{\int_{-\infty}^{\infty} |E_y|^2 \, dz} \tag{2.1}$$

where E_y the electric field in the direction perpendicular to the junction plane.

GRIN-SCH waveguide consists of a high-index low-energy-gap active layer sandwiched between optical confining layers, which are in turn surrounded by waveguide cladding layers. The index profile of the GRIN-SCH waveguide is shown in Fig. 2-2. The confining layers generally have a nonuniform index of refraction which might vary in a parabolic or linear manner. The square of the index of refraction is assumed to be linear in the confining layer. This form is used so that Airy function solutions may be used in the graded region. The differences between a square of the index and a linearly varying index should be negligible for most practical situations, since the index differences between layers are small.

Since most multiheterostructure lasers operate with electric fields in the plane of the layers, we will calculate only such TE modes. The general field equation is

$$\frac{dE^2}{dz^2} + (n^2k^2 - \beta^2)E = 0 \qquad (2.2)$$

where a common time- and space-dependent factor of $\exp[j(\omega t-\beta x)]$ has been removed. The x-directional propagation coefficient β is the eigenvalue to be found, and the frequency $\omega = 2\pi c/\lambda$. The index in the graded regions indicated in Fig. 2-2 are

$$\begin{array}{lll} nz = (n_3^2 - n_2^2)(z-d/2)/w + n_2^2 & d/2 < z < d/2+w, & \\ \quad\;\;\; (n_2^2 - n_3^2)(z+w+d/2)/w + n_3^2 & -w-d/2 < z < -d/2 & (2.3) \end{array}$$

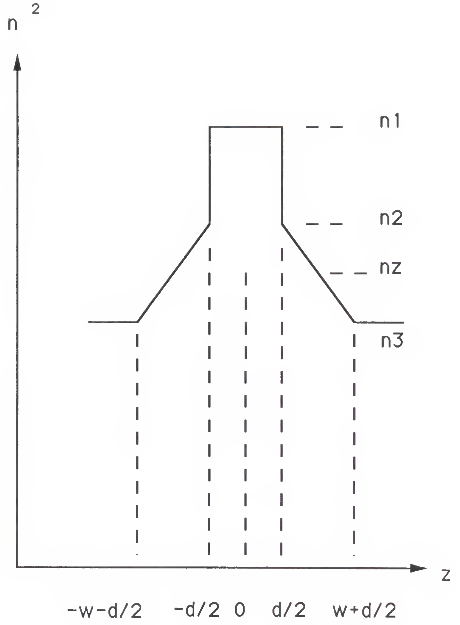

Fig. 2-2. Spatial profile of the square of the index of refraction for a GRIN-SCH waveguide. n1=n_1^2, n2=n_2^2, and n3=n_3^2

The non-normalized fields in the three regions are

$$E_y = F_a \exp(i\tau_a z) + G_a \exp(-i\tau_a z) \qquad -d/2 < z < d/2,$$
$$E_y = F_b \, Ai(t) + G_b \, Ai(t) \qquad d/2 < z < d/2+w$$
$$E_y = G_c \exp[-\tau_c(z-d/2-w)] \qquad d/2+w < z \qquad (2.4)$$

The factors in the arguments of Eq.(2.4) are

$$\tau_a = (n_1{}^2k^2 - \beta^2), \ \ \tau_c = (\beta^2 - n_1{}^2k^2),$$
$$t=\phi^{1/3}(z-\zeta), \ \phi=(n_2{}^2 - n_3{}^2)k^2/w, \ \zeta= (\phi d/2 + n_2{}^2k^2 - \beta^2)/\phi,$$
$$k = 2\pi/\lambda, \qquad (2.5)$$

and the functions Ai and Bi are the standard Airy functions [Abra72]. The boundary conditions are the TE fields and their derivative should be continuous at $z = d/2$ and $z = w + d/2$. Derivative of the field at $z = 0$ are zero. When these boundary conditions are applied to Eq.(2.4), this produces five equations linear in the unknown coefficients F_a, F_b, G_a, G_b, and G_c, with functional arguments dependent on the coefficient β. After eliminating F_a, F_b, G_a, G_b, and G_c, the resulting eigenvalue equation is

$$\tan\left(\frac{\tau_a d}{2}\right) = \left(\frac{\tau_c}{\tau_a}\right)\frac{F_1 + F_2}{F_3 + F_4} \qquad (2.6)$$

where
$$F1 = -Ai'(ac)\,Bi(cc) + Ai(cc)\,Bi'(ac),$$
$$F2 = (\phi^{1/3}/\tau_c)[Ai'(cc)Bi'(ac) - Ai'(ac)Bi'(cc)],$$
$$F3 = Ai(ac)Bi'(cc) - Ai'(cc)Bi(ac)],$$
$$F4 = (\tau_c/\phi^{1/3})[Ai(ac)Bi(cc) - Ai(cc)Bi(ac)],$$
$$ac= \phi^{1/3}(d/2- \zeta), \text{ and } cc = \phi^{1/3}(d/2+w-\zeta) \qquad (2.7)$$

The primed functions are spatial derivatives. In numerical calculation, we used IMSL libraries AI, BI, AID, and BID for the Airy functions and its derivatives. The parameters used for this structures are $n_1=3.62$, $n_2=3.4$, $n_3=3.1$ [Case78], w=0.2 μm, and $\lambda=0.88$ μm. In Fig. 2-3 is shown plot of confinement factor Γ as a function of active layer thicknesses from 5 nm to 40 nm.

2.3. Measurement

Three different wafers with the structure shown in Fig. 2-1 were used. The only variable between the three wafers was the active layer thickness d which was 7.5 nm (SQW lasers) , 20 nm, and 40 nm (bulk lasers). Oxide stripe lasers were fabricated from each wafer with a stripe width W of 150 μm and cavity length L values ranging from 250 μm to 1000 μm. The facets were uncoated and only lasers with uniform near fields were used. The measurement set-up is shown schematically in Fig. 2-4. The samples were measured with pulsed power supply. With the copper block held at a certain temperature, output power/current profiles were generated using 200 nm-wide drive pulses. Temperature was controlled by changing the voltage applied to the heating element and monitored by temperature indicator.

For a precise determination of threshold current (I_{th}), the spectrum of each laser was observed as a function of current (low duty cycle pulsed operation). The differential quantum efficiency (η_d) of each laser was measured from the slope of the output power (P_o) vs. current (I) characteristic. Internal loss coefficient α_i and carrier injection efficiency η_{in} shown in Table I were determined from η_d vs.

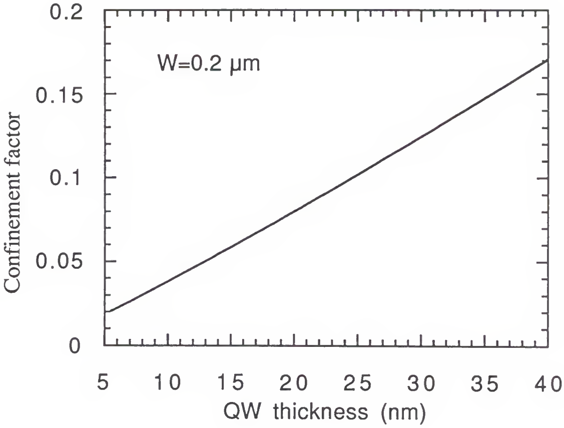

Fig. 2-3. Optical confinement factor Γ as a function of active layer thickness d for the GRIN-SCH trangular well waveguide.

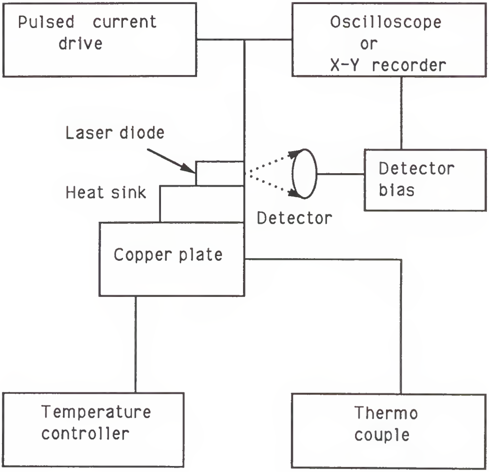

Fig. 2-4. The schematic of the threshold current measurement set-up

L measurements [Zmud91]. The measured values of J_{th} are given in Table II [Zmud91]. Figs. 2-5 and 2-6 show the η_d^{-1} vs L measurement data for the 40 nm and 7.5 nm QW respectively. The peak of the mode gain at threshold is given by the total cavity loss $G_{th} = \Gamma g_{th} = \alpha_i + \frac{1}{L}\ln\frac{1}{R}$, where R is the mirror reflectivity (0.32) at facet, and L is the device length. The material peak gain at threshold, g_{th}, was calculated using the relation between mode gain and active layer material gain, $G_{th} = Gg_{th}$.

2.4. Prediction of J_{th} and T_0

For the prediction of the threshold current density and characteristic temperature at 25°C, a detailed, published CZR model [Chin88, Chin89] was used. Important features included in the Chinn model are as follows: carrier scattering, gain anisotropy, Γ band non-parabolicity, energy levels of GRIN layer, L and X type carriers, band gap renormalization, carrier leakage from GRIN layer, light hole subband nonparabolicity, nonradiative processes by carrier leakage over the confining potential barriers and from the Auger recombination. For the prediction of threshold current density, we have used the G_{th} estimated in Table II for a given d and L.

The calculation of the peak gain requires a calculation of the spectral dependence of the mode gain from the gain equation, followed by spectral convolution to include the intraband carrier

Table. I

Measured values of η_{in}, α_i, and calculated values of Γ for lasers from each wafer

d (nm)	η_{in}	$\alpha_i(cm^{-1})$	Γ
7.5	0.82	7.0	0.030
20	0.90	8.5	0.081
40	0.98	13	0.180

Table. II

Measured values of J_{th} and calculated values of g_{th} and J_{th}/d

d (nm)	L(μm)	J_{th} (A/cm^2)	g_{th} (cm^{-1})	J_{th}/d (kA/cm^2-μm)	G_{th} (cm^{-1})
7.5	250	448	1752	59.7	52.6
"	500	239	992	31.9	29.8
"	750	178	738	23.7	22.2
"	1000	161	612	21.5	18.4
20	250	452	654	22.6	54.1
"	500	323	378	16.2	31.3
"	750	245	286	12.3	23.7
"	1000	212	240	10.6	19.9
40	250	467	335	11.7	60.6
"	500	371	205	9.28	37.1
"	750	319	161	7.98	29.1
"	1000	277	139	6.93	25.2

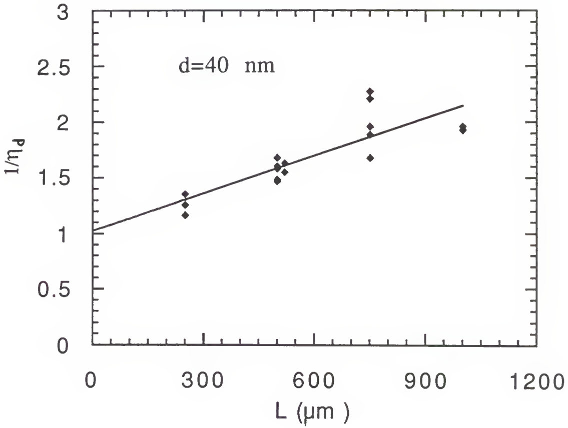

Fig. 2-5. Reciprocal of the external differential quantum efficiency ($1/\eta_d$) vs cavity length for 40 nm GRIN-SCH-SQW at 25°C.

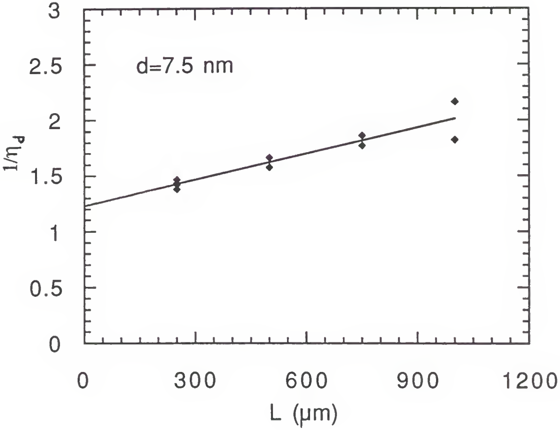

Fig. 2-6. Reciprocal of the external differential quantum efficiency ($1/\eta_d$) vs cavity length for 7.5 nm GRIN-SCH-SQW at 25°C.

scattering. The sharp-featured curve represents the unconvolved spectra, and the corresponding curve of the dotted line type represents the convolved spectra in Fig 2-7. The model gain has been calculated using the product of the optical confinement factor times the material gain coefficient evaluated at the curve's spectral peak. Each curve is associated with a well-defined carrier density.

In order to make a correspondence between carrier density and measurable current density (proportional to carrier generation rate), we must include all of the subthreshold carrier recombination processes, sum their rates, and equate them to the carrier injection rate. The radiative component of the excitation current density at the various drive levels is found from the integral over energy of the total spontaneous emission spectrum. An example of such a calculated spectrum is shown in Fig.2-8, broadened by the addition of intraband scattering. Nonradiative components of the current density include contributions from indirect-gap nonradiative recombination, Auger recombination, and leakage of carriers over the confining energy barriers. The radiative and nonradiative recombination rates can all be calculated for each value of carrier density. Since the peak gain is a function of carrier density, each value of peak gain can be associated with a current density whose components can be added sequentially for modeling purposes, to examine their relative sizes. The carrier density, while a necessary variable for the model, does not appear in the final result for the peak mode gain G as a function of current density J (Fig. 2-9). T_0 can be predicted simply by calculating G(J) at several temperatures, and

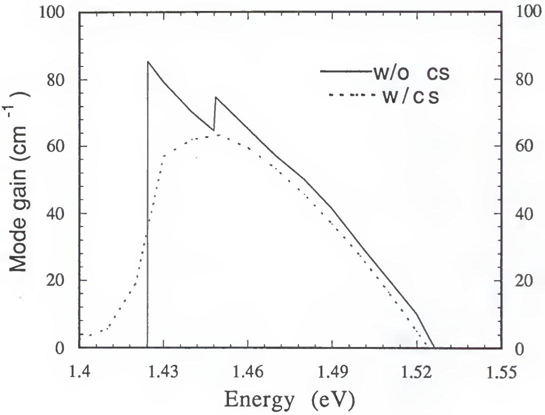

Fig. 2-7. TE mode gain as a function of energy for a GRIN-SCH-SQW laser. Unconvolved: dashed line and convolved: dotted line.

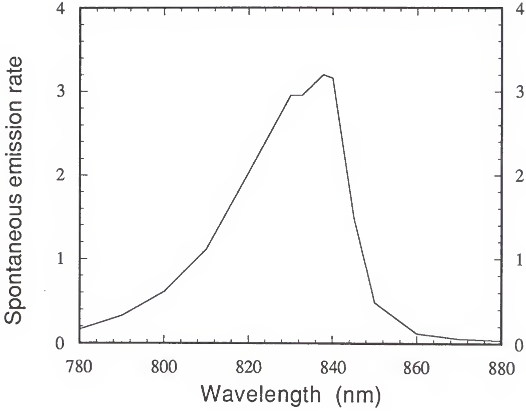

Fig. 2-8. Calculated total spontaneous emission spectral density (10^{15} cm^{-2} sec^{-1} nm^{-1}) as a function of wavelength. The spectrum has been convolved.

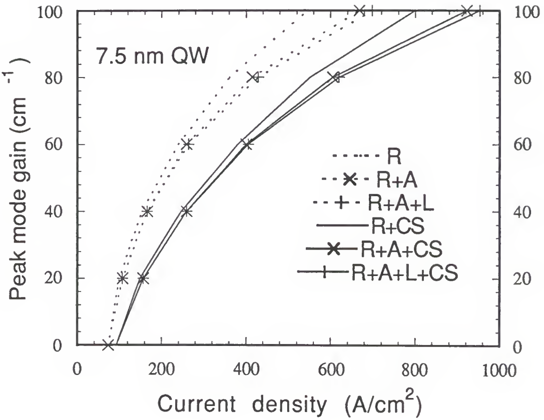

Fig. 2-9. Peak TE mode gain as a function of current density. The dashed curves, from unconvolved spectral gains, are calculated for radiative recombination(R), radiative plus Auger recombination(R+A), and radiative and Auger recombination plus carrier leakage(R+A+L) over the potential barriers. The corresponding solid curves come from spectrally convolved gains. CS is carrier scattering.

finding the required threshold current density at those temperatures for a specified threshold gain. The T_0 was obtained from the exponential variation of J_{th} with temperature, $J(T)=J(T_r)\exp[(T-T_r)/T_0]$, where T_r is the arbitrary reference temperature, in the range 25°C - 70°C. The predicted peak mode gain vs current density and T_0 vs QW thickness are shown in Figs. 2-10 and 2-11.

2.5. Results and discussion

We compared the measured G_{th} vs J_{th} with predicted one for the d=7.5 nm, 20 nm and 40 nm QW in Fig.2-12. In 20 nm and 40 nm QW, theoretical J_{th} is uniformally overestimated, while in 7.5 nm, experimental values are close to the prediction for long lasers (750 and 1000 μm). However, theory starts to deviate from the experiment as L shortens (250 and 500 μm). Threshold current density as a function d for L=500 μm are shown in Fig.2-13. For the theoretical mode gain estimation, we used α_i values in the intermediate well size interpolated linearly from the measured α_i values. In Fig.2-14 we plotted characteristic temperature (T_0) as a function of quantum well thickness d for these structures. Predicted T_0 values agree pretty well with experimental values but are overestimated because J_{th} is not predicted properly. There is a general tendency for T_0 to increase, as shown in Fig. 2-14, as quantum well thickness increases [Hers84]. Thick QW diode lasers are favored for the high temperature operation from the T_0 point of view. T_0 is a very complicated parameter as found by several authors. Experimental work indicates that T_0 is actually decreasing

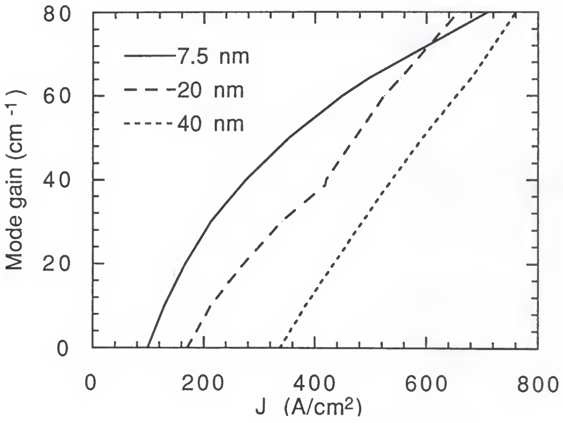

Fig. 2-10. Peak TE mode gain as a function of current density for a GRIN-SCH-SQW laser as a function of quantum well thickness.

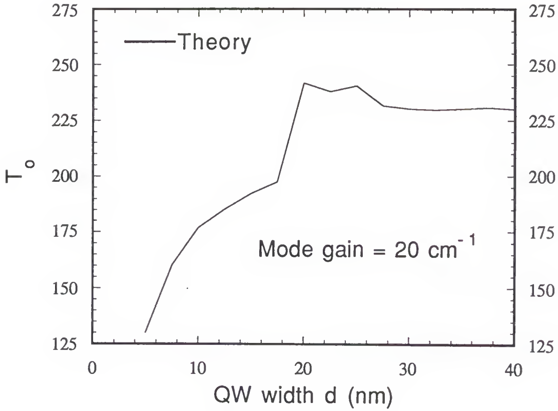

Fig. 2-11. Characteristic temperature of GRIN-SCH-SQW laser as function of quantum well thickness.

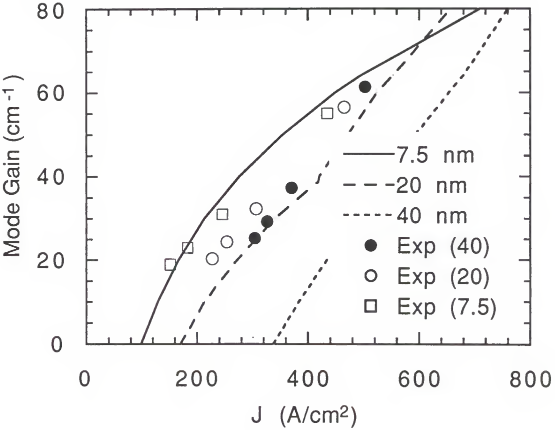

Fig. 2-12. Comparison of measured and theoretical mode gain vs current density for a GRIN-SCH-SQW laser as a function of quantum well thickness .

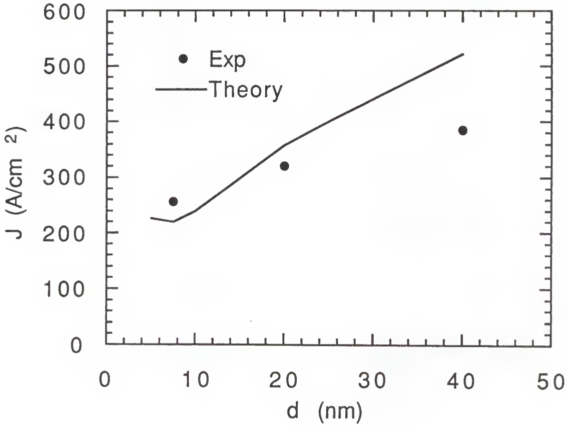

Fig. 2-13. Comparison of measured and theoretical mode gain vs current density as a function of QW thickness for GRIN-SCH-SQW laser with cavity length L=500 μm and stripe width W=150 μm diode.

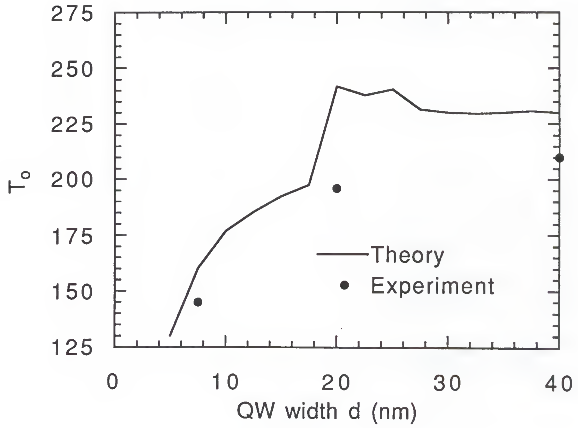

Fig. 2-14. Comparison of measured and theoretical characteristic temperature (T_o) as a function of QW thickness for cavity length L=500 μm and stripe width W=150 μm diode laser.

function of temperature [Zory86a, Shea87]. Also it has been found that T_0 for a GRIN-SCH-SQW increases with cavity length [Zory86b, Leop87]. T_0 is very bad parameter. Therefore we do not study T_0 anymore in this thesis.

The possible reasons why the CZR model do not agree with experiment are as follows: (i) CZR model breaks down for the thick well (bulk). (ii) Lineshape function, which was assumed to be independent of well thickness, temperature, carrier energy and carrier density, is not appropriate. (iii) Nonradiative current might not be estimated correctly. (iv) CZR model does not treat the valence band correctly. Fundamental studies [Cola87, Ahn88] have shown that the valence band structure of quantum wells deviate significantly from that of the parabolic band due to VBM as the QW width decreases. VBM gives nonparabolic bands which affect both the minimun confinement energies and the density of states functions. The density of states functions are found to differ considerably from the the simple step-like shape computed from the band edge effective masses. The band mixing also results in large differences in the momentum vector dependence of the matrix elements, and moreover, some of the transitions which were previously assumed to be forbidden become partially allowed. The quantum well gain calculated by the k.p method and k-selection rules clearly show the effects of band mixing both in shape and in peak magnitude. These results are considerably different than those obtained from the conventional methods with parabolic bands and with matrix elements which have constant total magnitude. The threshold current in a QW laser is found to be strongly underestimated if band mixing effects are ignored. Although the effects of the band-mixing on the band structure and gain of a QW have been studied [Cola87, Ahn88, Zory92], very little work has been done on the comparison of theory with the experimental data.

2.6. Suggestion

To sort out the problem, we chose two cases, thick 40nm well (bulk) and thin 7.5 nm QW. In thick well all the complicated phenomena related to the QW vanish and only CS is expected to be fundamental. We investigated the CS effect on J_{th} using standard bulk theory [Ster73]. In thin 7.5 nm QW where quantum size and nonradiative effects are important, we studied the CS effects on J_{th} using VBM QW theory. In the new model, the leakage current was included into the total current in terms of spontaneous emission efficiencies (η_{sp}), which can be expressed as the product of two efficiencies, η_{in} = injection efficiency and η_r = active layer radiative efficiency [Zory91, Lim91].

CHAPTER 3
FITTING THICK QW DATA WITH STANDARD BULK THEORY

3.1. Introduction

Threshold current density J_{th} predictions for diode lasers are based on a knowledge of the relationship between mode gain G and current density J for the laser of interest. In order to demonstrate the validity of a given G-J relation, one usually performs experiments on simple, wide stripe lasers where complications due to current spreading, lateral mode overlap and antiguiding can be minimized. In this case, G can be expressed as the product of a transverse mode confinement factor Γ and peak material gain g. Mode gain at threshold, G_{th}, can then be expressed in the form [Chin88],

$$G_{th} = \Gamma g_{th} = \alpha_i + \frac{1}{L} \ln \frac{1}{R} \qquad (3.1)$$

where α_i is the mode loss coefficient, L is the cavity length and R is mode facet reflectivity. Since one can estimate Γ, α_i and R with fair accuracy for a given resonator, one can estimate g_{th}.

To find the J_{th} value associated with the estimated g_{th} value, one usually uses a strict k selection theory and a carrier scattering (CS) convolution procedure [Chin88]. If one knows the CS function, one can calculate the value of carrier density N which yields g_{th}. This value of $N = N_{th}$ is then used to compute the spontaneous recombination rate density at threshold $(R_{sp})_{th}$ which is related to J_{th} by

$$J_{th} = \frac{ed(R_{sp})_{th}}{\eta_{sp}} \tag{3.2}$$

In this equation, e is the electron charge, d is the active layer thickness and η_{sp} is the efficiency for converting J into spontaneous emission in the active layer.

In experimental situations where threshold gain requirements are high (for example when the active layer temperature T is high, L is short or d is very thin), it is difficult to estimate η_{sp} [Chin88]. However, if we choose T low, L long and d thick, then η_{sp} should be $\cong$ 1, provided the laser material being used is good. The MOCVD laser material [Dapk82] used in this work is shown in Fig. 2-1. It is a linearly graded refractive index (GRIN), separate confinement heterojunction (SCH), single potential well (SW) structure with an active layer thickness d = 40 nm. The GRIN layers on either side of d are 0.2 μm thick with aluminum grading from 30% to 70%. The p and n doped cladding layers have 70% aluminum and are 1.5 μm thick. The value of G for this structure is the product of the geometrical overlap factor (0.164) times a correction factor of 1.1.

3.2. Predictions

Fig. 3-1 and 3-2 show calculated plots of g_{th} vs J_{th}/d at T = 25 °C and 125 °C, respectively, without CS convolution ($\equiv g_o$) and with CS convolution ($\equiv g_c$). The convolution function (L) used in this case is

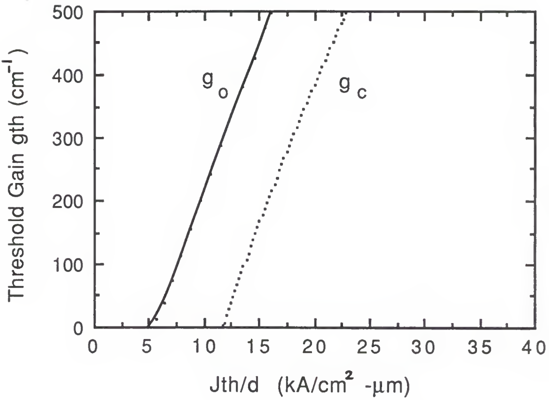

Fig. 3-1. Threshold gain as a function of J_{th}/d at 25°C. Solid curve is without CS convolution (g_o) and dashed curves is with CS convolution (g_c). m* in matrix element is $0.053m_o$. η_{sp} is assumed to be 1.

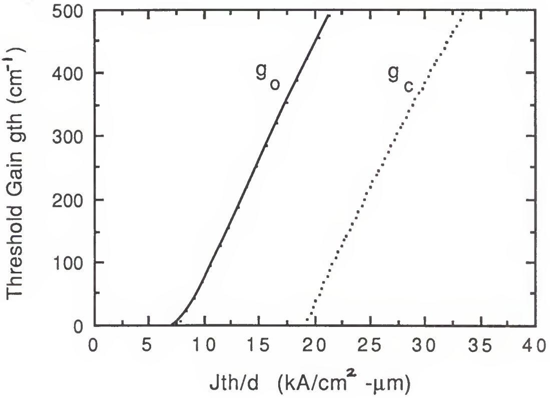

Fig. 3-2. Threshold gain as a function of J_{th}/d at 125°C. Solid curve is without CS convolution (g_o) and dashed curves is with CS convolution (g_c). m* in matrix element is $0.053m_o$. η_{sp} is assumed to be 1.

Lorentzian with a width γ_{cv} which depends on photon energy hν and active layer temperature T [Yama81, Asad89] :

$$L = L(h\nu\ ,T) = \frac{1}{\pi}\ \frac{\gamma_{cv}}{(h\nu - E_{cv})^2 + \gamma^2_{cv}} \tag{3.3}$$

where $\gamma_{cv} = \gamma_{cv}(h\nu,T) \equiv \dfrac{\hbar}{\tau_{cv}\ (h\nu,T)}$. Band edge scattering times $\tau_{cv}(h\nu = E_g, T)$ of 0.1 ps at 25 °C and 0.055 ps at 125 °C were used to compute the g_c curves in Figs. 3-1 and 3-2. E_{cv} is the photon energy at which the convolved gain is calculated when integrating the convolution integral over values of hν from E_g to ∞.

The expression for spectral gain g(hν,T) that is convolved with Eq. (3.3) to determine the g_c curve (no convolution for the g_o curve) is [Yan90] :

$$g(h\nu,T) = \frac{1}{h\nu}\frac{e^2 h}{2\varepsilon_o c \tilde{n} m_o}\ |M_o|^2 \rho_{rd}\ (f_c - f_v) \tag{3.4}$$

where $\tilde{n}$ is a refractive index parameter, $|M_o|^2$ is the transition matrix element given by

$$|M_o|^2\ = m_o\left(\frac{m_o}{m^*}\ -1\right)\frac{E_g(E_g+\Delta)}{6\left(E_g+\frac{2\Delta}{3}\right)} \tag{3.5}$$

where E_g = energy band gap, Δ = split-off valence band separation, and ρ_{rd} is the reduced density of states with spin degeneracy factor of 2 included given by

$$\rho_{rd} = \frac{8\sqrt{2}\pi m_r^{3/2}}{h^3} (h\nu - E_g)^{1/2} \qquad (3.6)$$

The value for $(R_{sp})_{th}$ used to determine J_{th} in Eq.(3.2) is calculated by using N_{th} in the following [Yan90] :

$$(R_{sp})_{th} = \int_{E_g}^{\infty} [r_{sp}(h\nu,T)]_{th}\, d(h\nu) = \frac{4\pi e^2 \tilde{n}'}{\varepsilon_o h^2 c^3 m_o^2} |M_o|^2 \int_{E_g}^{\infty} h\nu\, \rho_{rd}\, f_c(1-f_v) d(h\nu) \qquad (3.7)$$

Effective masses used in these calculations [Corz90] were $m_c = 0.067m_o$, $m_{hh} = 0.59m_o$ and $m_{lh} = 0.083m_o$. The value of m^* used in Eq. (3.5) was $0.053m_o$ [Yan90] and the value of $\tilde{n}$ and $\tilde{n}'$ in Eqs. (3.4) and (3.7) was 3.6. Split-off valence band separation was 0.33 eV.

It is interesting to note that if we change η_{sp} in the 25 °C g_o curve of Fig. 3-1 from 1 to 0.61, it closely approximates the convolved curve (g_c) where $\eta_{sp} = 1$. For the 125 °C curve, $\eta_{sp} = 0.54$ achieves the same result. It is clear, therefore, that one must know η_{sp} if one is to utilize this method to determine the correct CS convolution function. As mentioned earlier, we chose to use relatively thick active layer material in this work (d = 40 nm) so that we could make the $\eta_{sp} = 1$ assumption with some confidence when comparing measured J_{th} data of long lasers at low temperature with theory. The validity of this assumption is discussed below.

3.3. Results and discussions

In the previous section, we showed that the G-J relation when applied to the wide stripe lasers described earlier, can be transformed to the g_{th} - J_{th}/d relations shown in Figs. 3-1 and 3-2. Fig. 3-3 is the same plot as Fig. 3-1 with the experimental data points added. The experimental g_{th} values shown are determined using Eq. (3.1) and measured α_i values deduced from differential quantum efficiency measurements vs L. The error bars on the g_{th} points represent the possible variation in g_{th} due to uncertainties associated with G, α_i and R. The error bars on the J_{th}/d points represent the possible variation in I_{th} from chip to chip and uncertainty in amount of current spreading. The lowest point represents the L = 1000 µm lasers and the highest represents the L = 250 µm lasers. As shown, the calculated g_o curve overestimates the value of J_{th} by about 8% whereas the g_c curve overestimates J_{th} by about 78%. In this case, it is impossible to fit the g_o curve to the experimental points by making $\eta_{sp} < 1$, since this approach moves the g_o curve to the right. It is also impossible to fit the g_c curve to the data since g_c is always to the right of g_o. If the expression for $|M_o|^2$ in Eq.(3.5) is modified by using $m^* = 0.067m_o$ rather than $0.053m_o$, the recalculated g_o curve (g_o') shown in Fig. 3-4 is to the left of the experimental points. In this case, if one uses $\eta_{sp} = 0.98$ in the expression for J_{th} (Eq.(3.2)), g_o' fits well with the data. The g_c curve of course has no chance to fit the data unless $\eta_{sp} > 1$, prohibited by definition. In order to determine if $\eta_{sp} = 0.98$ is reasonable, we utilized the fact that η_{sp} can be expressed as the product of two efficiencies, $\eta_{in} \equiv$ injection efficiency

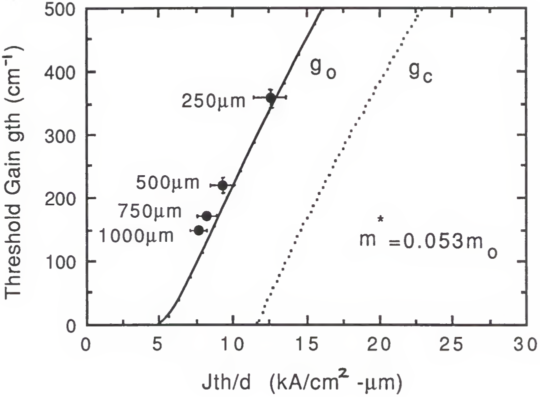

Fig. 3-3. Threshold gain as a function of J_{th}/d at 25°C with $m^*=0.053m_o$ in matrix element. Solid curve is without CS convolution (g_o) and dashed curves is with CS convolution (g_c). η_{sp} is assumed to be 1.

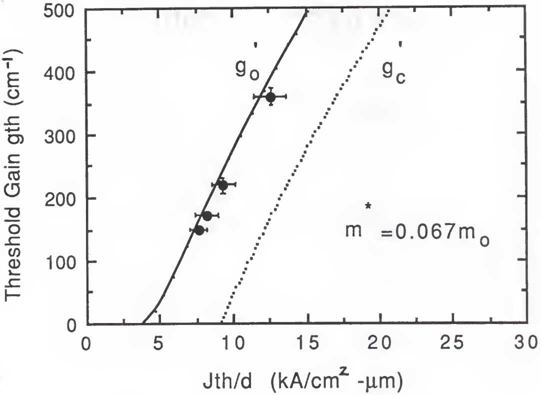

Fig. 3-4. Threshold gain as a function of J_{th}/d at 25°C with $m^*=0.067m_o$ in matrix element. Solid curve is without CS convolution (g_o) and dashed curves is with CS convolution (g_c). η_{sp} is assumed to be 1.

and $\eta_r \equiv$ active layer radiative efficiency [Zory91]. From differential quantum efficiency (η_d) vs L measurements, we determined that η_{in} η_{sp} is assumed to be 1.$\cong$ 0.98, implying that $\eta_r \cong 1$. Since $\eta_r \equiv R_{sp}/(R_{sp}+R_{nr})$ where R_{nr} is the non-radiative recombination rate density in the active layer at threshold, $\eta_r \cong 1$ implies $R_{nr} \cong 0$, not unreasonable for high quality diode laser material at low carrier densities.

The justification for making the particular modification to $|M_o|^2$ described above is essentially historical in that the resulting g_o' curve is the same as would be predicted using Stern's k-selection formalism [Ster73]. In reviewing how well Stern's theory compared to experiment, Thompson [Thom80] pointed out that it predicted J_{th} values somewhat lower than that measured for their best lasers. About the same time (early '80s), Yamada pointed out that Stern's theory did not take CS into account implying that Stern's g(hν) function was too optimistic. By convolving the g(hν) function with a Lorentzian broadening function (CS time of about 10^{-13} sec), Yamada and Ishiguro were able to fit their data [Yama81]. On the other hand, Garbuzov et al [Garb87] showed good agreement with J_{th} values measured by Hakki and Paoli with a carrier scattering time of about 10^{-12} sec (CS contribution small). The essence of the above history appears to be that if measured J_{th} values are low enough, Stern's theory without CS is sufficient to explain results.

Fig. 3-5 shows the calculated g_o' curve at T = 125 °C for $\eta_{sp} = 1$ along with the measured 125°C data. Since the data points are to the right of the predicted curve, one can fit the data by using CS, $\eta_{sp} < 1$ or a combination of both. Fig. 3-6 shows that if we choose $\eta_{sp} = 0.74$,

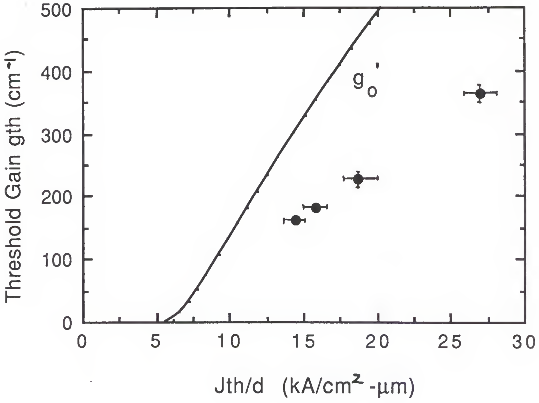

Fig. 3-5. Threshold gain as a function of J_{th}/d without CS convolution at 125°C with $\eta_{sp} = 1$. m* in matrix element is $0.067 m_o$.

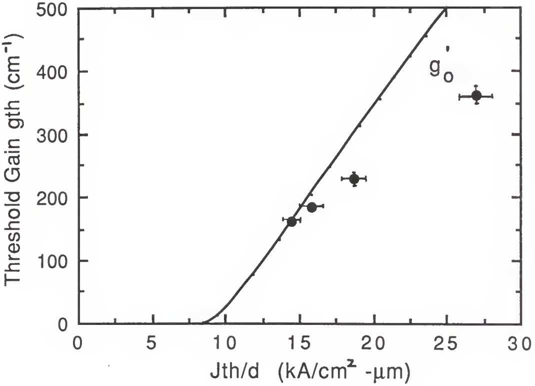

Fig. 3-6. Threshold gain as a function of J_{th}/d without CS convolution at 125°C with η_{sp} =0.74. m* in matrix element is $0.067m_o$.

the $L = 1000\ \mu m$ point falls on the g_o' curve. From the slope efficiency data for lasers with L = 500, 750 and 1000 μm at T = 25 °C, we determined that $\eta_{in} = 0.78$ at 125°C (see Appendix A), very close to the value for η_{sp} (=0.74) required to fit the $L = 1000\ \mu m$ data point. In this case, g_o' "predicts" the measured J_{th} values using $\eta_{in} = 0.78$, $\eta_r = 0.95$ for the 1000 μm laser and decreasing η_r for the shorter lasers. This dependence of η_r on g_{th} is very reasonable since nonradiative recombination (e.g. Auger recombination) can be expected to lower η_r as g_{th} and N_{th} increase. Fig. 3-7 shows the g vs J_{th}/d with fixed $\eta_{in} = 0.78$ and variable η_r. Radiative efficiency was calculated from the ratio of the radiative recombination rate and Auger recombination rate. A better fit to the data may be obtained if exact η_{in} for each cavity length lasers are used. Based on these results, it appears that if facet coatings had been used to lower the required N_{th} for these lasers, then it would have been a good approximation to use $\eta_r = 1$ for the 500 and 750 μm long lasers, even at 125°C. In that case, we would then only have to know how to predict the value of η_{in} at 125°C in order to predict J_{th} at 125 °C. Since η_{in} is related in a simple way to η_d for lasers where output power vs drive current is a straight line [Zory91], the ability to predict η_{in} also allows a prediction of η_d. Consequently, if CS can be ignored, then the problem of predicting J_{th} and η_d at any temperature reduces to the problem of predicting the temperature dependence of η_{in}.

As mentioned above, since the 125 °C data points of Fig. 3-5 are to the right of the g_o' curve with $\eta_{sp} = 1$, it may be possible to

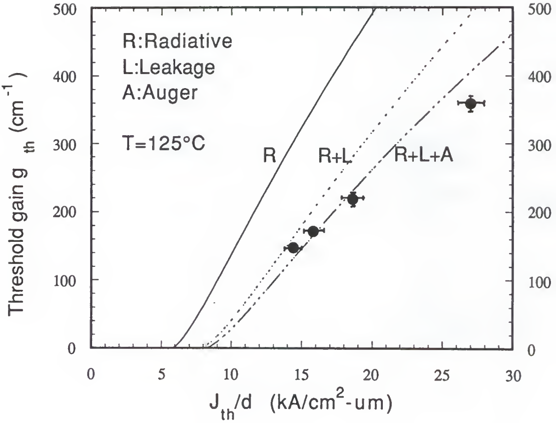

Fig. 3-7. Threshold gain as a function of J_{th}/d without CS convolution at 125°C with $\eta_{in} = 0.78$ and η_r variable. m* in matrix element is $0.067m_0$.

include CS and still fit the data since CS will shift the curve to the right. However, since the measured value of η_{in} is 0.78, one must set $\eta_{sp} \leq 0.78$, which means the difference between the data points and the curve of Fig. 3-6 actually indicates whether or not CS can be used to fit the data, not the difference between the data points and the curve in Fig. 3-5. Since including CS will shift the curve in Fig. 3-6 substantially to the right, no fit can be obtained at 125 °C if CS is included. Therefore, it is not possible to fit either the 25 °C data or the 125 °C data if CS is included. The only way to include CS and fit the data with allowed values of η_{sp} is to modify the expressions for gain and spontaneous emission in Equations (3.4) and (3.7). For example, if a factor of 1/2 is introduced on the right-side of both Equations (3.4) and (3.7), a good fit using the "accepted" bandedge CS time of 0.1 ps can be obtained at T = 25 °C with $\eta_{sp} = 1$.

3.5. Summary

In summary, threshold current density predictions were made for GaAs/AlGaAs GRIN-SCH-SW diode lasers with 40 nm thick active layers at 25 °C and 125 °C. A reasonable fit to the experimental data at both temperatures was obtained without including CS. Standard bulk theory combined with measured carrier injection efficiency (η_{in}) was used.

APPENDIX A
CARRIER INJECTION EFFICIENCY AT 125°C

Carrier injection efficiency (η_{in}) is determined from the differential quantum efficiency (η_d) vs L measurements. However, it is difficult to estimate h_{in} in experimental situations where threshold gain requirements are high (for example when the active layer temperature T is high). Therefore we deduce h_{in} from the following simple relationship, $\eta_d=\eta_{in}\eta_o(\alpha_i)$, where η_o is the external quantum efficiency defined by

$$\eta_o = \frac{1}{2}\,\frac{\ln \frac{1}{R}}{\alpha_i L + \ln \frac{1}{R}} \tag{A.1}$$

The differential quantum efficiency ratio between 125°C and 25°C can be rewritten as follow for facet mirror reflectivity R=0.32

$$\frac{\eta_d(125°C)}{\eta_d(25°C)} = \frac{\eta_{in}(125°C)}{\eta_{in}(25°C)}\,\frac{\alpha_i(25°C)L+1.2}{\alpha_i(125°C)L+1.2} \tag{A.2}$$

We assume that α_i is same for both at 25°C and 125°C. Then η_{in} at 125°C can be represented as the ratio of the diffenertial quantum efficiency for both temperature.

$$\eta_{in}(125°C) \cong \frac{\eta_d(125°C)}{\eta_d(25°C)} \qquad (A.3)$$

Fig.A-1 shows the η_{in} at 125°C as function of cavity length L.

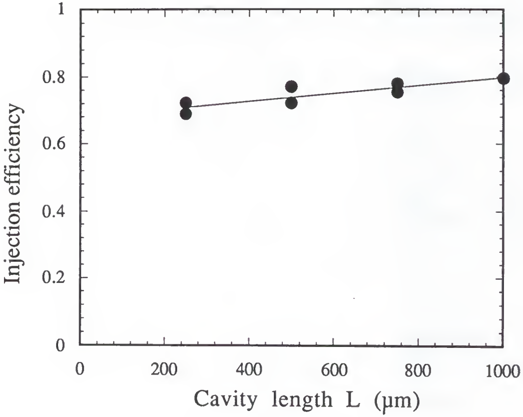

Fig. A-1. Injection efficiency as a function of cavity length L at 125°C.

CHAPTER 4
FITTING THIN QW EXPERIMENTAL DATA WITH NEW VBM QW THEORY

4.1. Introduction

Fundamental studies [Cola87, Ahn88] have shown that the valence band structure of quantum wells deviates significantly from that of the parabolic band due to valence band mixing as the QW width decreases. The valence band mixing gives nonparabolic bands which affect both the subbands energies and the density of states functions. (i) The density of states functions are found to differ considerably from the simple step-like shape computed from the band edge effective masses. (ii) The coupling of heavy and light hole results in large difference in the matrix element, and some of the transitions which were previously assumed to be forbidden are partially allowed. This phenomena not predicted by the parabolic model violate the $\Delta n = 0$ selection rule, where n is the principle quantum number.

The quantum well gain calculated by the k.p method and k-selection rules clearly show the effects of band mixing. These results are considerably different than those obtained from the conventional methods with parabolic bands and with matrix elements which have constant magnitude. The threshold current in a QW laser is found to be strongly underestimated if band mixing effects are ignored. Although the modification to spectral gain due to band-mixing has been discussed in the literature [Cola87, Ahn88, Corz91], very little work has been done on the comparison of theory with experiment. Using the same procedures as used in fitting bulk data, we fitted the thin 7.5 nm QW data with valence band-mixing QW theory.

The multiband effective-mass theory (k.p method) [Lutti55] was used to calculate the band structure and electron (or hole) wave functions of a quantum well. For simpilicity, we assume that the conduction and valence bands are decoupled, which is in fact a good approximation for wide-band-gap semiconductors such as GaAs [Sand87]. For the conduction band, a simple isotropic parabolic band is used. For the valence band, we used 4x4 Luttinger-Kohn Hamiltonian, the element of which are derived based on the k.p method. We used finite difference method to solve the multiband effective mass equations.

4.2. Valence band mixing quantum well theory

4.2.1. Effective mass equations

The theory of the k.p method in bulk semiconductor was introduced by Kane [Kane55] and has been applied successfully to bulk semiconductors by number of authors [Lutti55, Lutt56, Lawa71]. The formalism was extended to the study of thin films by S.S. Nedorezov [Nedo71], and recently has been used in the study of quantum well structures [Faso84, Sand85, Chan85, Cola87, Ahn88, Corz90]. This approach has the virtue of being relatively simple and yet takes into account the important aspects of the strong hole interaction near the zone center. The formalism allows determination of the shape of the energy bands in the neighborhood of k=0 through symmetry considerations and an empirical fit of the effective masses. In this method, the wavefunctions of the QW are expanded in the wave functions of both constituent materials around the k=0 point. The resulting Hamiltonian for the slowly varying part of the wave function, the envelope function, can be described by the corresponding k.p matrix in each constituent material.

The subband structure of a quantum well is obtained by solving the Schroedinger equation.

$$H_0\Psi = [\frac{p^2}{2m_0} + V(r)]\,\Psi = E\Psi, \qquad (4.1)$$

where p is the momentum operator, H_0 is the perfect crystal Hamiltonian and V(r) is the potential due to quantum confinement. Due to the periodicity of V(r), the solution of the above equation are given Bloch waves of the form

$$\Psi = e^{ik.r}\,u(k,r)\ , \qquad (4.2)$$

where k is the wavevector of the electron, and u is a Bloch function with the special property that it is periodic with the crystal lattice. In defining localized solutions of (4.1) such as those in quantum wells, it is useful to consider linear combinations of Bloch wave solutions in (4.2). Using an arbitrary set of expansion coefficients, A(k), we can express a spatially localized wavefunctions as [Zory92]

$$\Psi = A(k)\int e^{ik.r}u(k,r)\,d^3k \approx u(o,r)\int A(k)e^{ik.r}d^3k \equiv F(r)u(r) \qquad (4.3)$$

The above description of localized states is known as the envelope function approximation [Lutt55]. The schematic energy band structure of a GRIN-SCH-SQW is shown in Fig. 4-1.

For a non-degenerate energy band, such as the conduction band, it has been shown by Luttinger and Kohn [Lutt55] (using a k.p formalism) that an effective mass equation or Schroedinger-like equation for the envelope function, F_e, as defined in (4.3) can be given as

$$(H_c + V) = E_c F_e, \tag{4.4}$$

where the Hamiltonian for the conduction band is simply given by

$$H_c = -\frac{\hbar^2}{2m_c}\frac{d^2}{dz^2} \tag{4.5}$$

The Bloch functions have been removed from the equation, and the effect of the periodic potential arising from the crystal lattice is now replaced by a conduction band effective mass, m_c. In this approximation, the quantum well created by the interfacing of three materials of different band gap truly becomes of a textbook particle in a box problem with F as the wavefunction, and the material band edges as the potential, V.

The simplicity of the band structure in the conduction band of a quantum well relies on the assumption that the interaction with other energy bands is weak enough that we can treat it perturbatively by replacing that interaction with a conduction band effective mass.

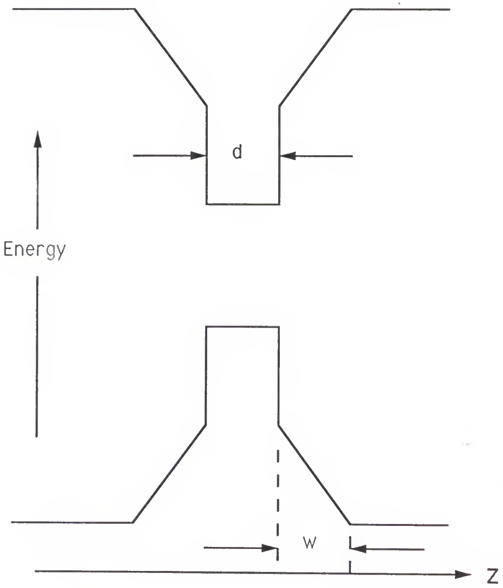

Fig. 4-1. Schematic energy band structure of a GRIN-SCH-SQW laser.

However, for bands degenerate in energy, the assumption of weak interaction is a poor one and cannot be used. Therefore, the effective mass equation (4.4) must be modified to include the strong degenerate band interaction. A modified derivation for the degenerate band effective mass equation has also been treated by Luttinger and Kohn [Lutt55]. In this case, we still obtain an effective mass equation for each degenerate band similiar to (4.4), however, as a result of the degeneracy, a coupling term is introduced which couples the equations together. For the degenerate HH and LH bands near the band edge, this implies that we must work with four coupled effective mass equations (we must include the spin degeneracy). Interaction between the HH and LH bands is by far the strongest, and we do not pay a large penalty by neglecting the other bands. The four coupled effective mass equations can be greatly simplifid using a method suggested by Broido and Sham [Broi85, Ahn88, Ahn90]. The two coupled effective mass equations for the degenerate bands can be expressed as [Zory92]

$$(H_h + V) F_h + W F_l = E_v F_h \tag{4.6}$$

$$(H_l + V) F_l + W^+ F_l = E_v F_l \tag{4.7}$$

where $F_{h,l}$ are the heavy and light hole envelope functions, and W^+ is the hermitian conjugate of W. Let choose the quantum well direction to be along z because the effective mass equations would not decouple at the band edge otherwise (see (4.11)). In this case, k_z is directed along the confinement axis and k_t is the transverse k vector component and lies in the plane of the well, as shown in Fig. 4-2.

Wave vectors k_z and k_t are two perpendicular k vector components, with k_z directed along a <100> direction, and k_t directed either along a <100> direction or a <110> direction within the plane of the well. With this, we can write [Zory92]

$$H_h = (\gamma_1 - 2\gamma_2)\, k_z^2 + (\gamma_1 + 2\gamma_2)\, k_t^2, \tag{4.8}$$

$$H_l = (\gamma_1 + 2\gamma_2)\, k_z^2 + (\gamma_1 - 2\gamma_2)\, k_t^2, \tag{4.9}$$

where

$$\gamma_1 - 2\gamma_2 \equiv \frac{\hbar^2}{2m_{hh}}, \gamma_1 + 2\gamma_2 \equiv \frac{\hbar^2}{2m_{lh}} \tag{4.10}$$

The material constants $\gamma_{1,2}$ are referred to as the Luttinger parameters [Lutt56], and are easily related to the HH and LH effective masses, m_{hh} and m_{lh} through (4.10). A third Luttinger parameter, γ_3, exists in the coupling term, W. The coupling term takes a slightly different form when k_t is directed along {100} and {110} directions [Zory92]. We can define the two forms as

$$W = \sqrt{3}\, k_t\, (\gamma_2\, k_t - i2\, \gamma_3\, k_z) \quad \text{for } \{100\} \text{ planes,} \tag{4.11a}$$

$$W = \sqrt{3}\, k_t\, (\gamma_3\, k_t - i2\, \gamma_3\, k_z) \quad \text{for } \{110\} \text{ planes.} \tag{4.11b}$$

Because the energy bands are different in the {110} and {100} plane, and because electrons will of course exist with k vectors in all planes, we use here the axial approximation [Alta85], which assumes $\gamma_2 = \gamma_3$ only in the W term.

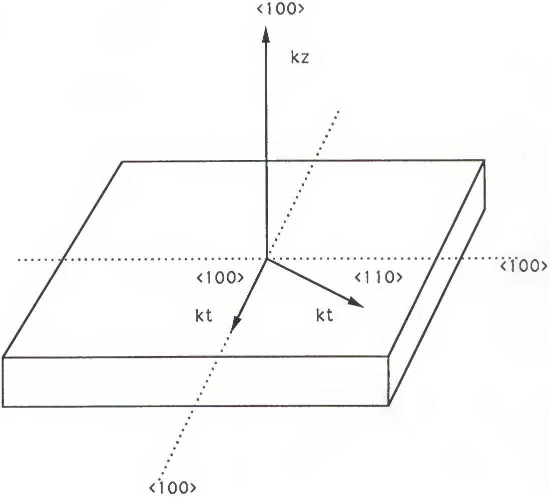

Fig. 4-2. Coordinate system used in the valence band model. The transverse or in-plane k vector, k_t, can be directed along either a <100> or <110> direction, whereas the confinement axis must be along a <100> direction.

From Eqs. (4.8)-(4.11), we have two coupled differential equations for $F_h(z)$ and $F_l(z)$ given by

$$[\,(\frac{1}{2}(\gamma_1+\gamma_2)\,k_t^2-\frac{1}{2}(\gamma_1-2\gamma_2)\frac{d^2}{dz^2})+\frac{m_o}{\hbar^2}V(z)\,]\,F_h(z)$$
$$+\,(\frac{\sqrt{3}}{2}\bar{\gamma}\,k_t^2-\sqrt{3}\,\gamma_3\,k_t\frac{d}{dz})\,F_l(z)\qquad=\frac{m_o}{\hbar^2}E_v\,F_h(z),\qquad(4.12a)$$

$$(\frac{\sqrt{3}}{2}\bar{\gamma}\,k_t^2+\sqrt{3}\,\gamma_3\,k_t\frac{d}{dz})\,F_h(z)+\;[\,(\frac{1}{2}(\gamma_1-\gamma_2)\,k_t^2$$
$$-\frac{1}{2}(\gamma_1+2\gamma_2)\frac{d^2}{dz^2})+\frac{m_o}{\hbar^2}V(z)\,]\,F_l(z)=\frac{m_o}{\hbar^2}E_v\,F_l(z),\qquad(4.12b)$$

It is convenient to normalize Eqs.(4.12a) and (4.12b) by defining

$$\xi=\frac{z}{L},\ \lambda_1=\frac{m_oL^2}{\hbar^2}E_v,\quad f=\frac{m_oL^2}{\hbar^2}\,V(\xi),$$
$$A_1=\frac{1}{2}(\gamma_1+\gamma_2)\,L^2k_t^2,\ A_2=\frac{1}{2}(\gamma_1-\gamma_2),$$
$$C=\frac{\sqrt{3}}{2}\bar{\gamma}\,L^2\,k_t^2,\ D=\sqrt{3}\,\gamma_3\,Lk_t\,,\ \bar{\gamma}=\frac{1}{2}(\gamma_2+\gamma_3)$$
$$B_1=\frac{1}{2}(\gamma_1-\gamma_2)\,L^2k_t^2,\ \text{and}\ \ B_2=\frac{1}{2}(\gamma_1+\gamma_2).\qquad(4.13)$$

Then Eqs.(13.a) and (13.b) become

$$(A_1-A_2\frac{d^2}{d\xi^2}+f(\xi))\,F_h(\xi)\;+\;(C-D\frac{d}{d\xi})\,F_l(\xi)$$
$$=\lambda_1\,F_h(\xi)\qquad(4.14a)$$
$$(C+D\frac{d}{d\xi})\,F_h(\xi)+(B_1-B_2\frac{d^2}{d\xi^2}+f(\xi))\,F_l(\xi)$$
$$=\lambda_1\,F_l(\xi)\qquad(4.14b)$$

By the same procedures, conduction band effective mass equation (4.4) becomes

$$\left(-\frac{1}{m_c}\frac{d^2}{d\xi^2} + \frac{2m_oL^2}{\hbar^2}V(\xi) + \frac{k_t^2L^2}{m_c} \right) F_c(\xi) = \frac{2m_oL^2}{\hbar^2} E_c F_c(\xi) \qquad (4.15)$$

where $m_c = m_c^*/m_o$, and E_c is the conduction subband energy.

4.2.2. Transition matrix element.

The transition of the optical matrix elements depend on the polarization of the incident light and we consider two cases: TE and TM. The transition matrix element can be simplified in terms of normalized envelope wavefunction

$$|M_T|^2 = |M_o|^2 \left[\frac{4}{3} |<F_l \mid F_c>|^2 \right] \qquad \text{TMpolarization} \qquad (4.16)$$

$$|M_T|^2 = |M_o|^2 \left[|<F_h \mid F_c>|^2 + \frac{1}{3} |<F_l \mid F_c>|^2 \right] \qquad \text{TE polarization} \qquad (4.17)$$

where $|M_o|^2$ defined in Eq.(3-8) is the bulk material transition matrix element. Here we used $m^* = 0.053m_o$ in $|M_o|^2$ for QW [Yan90]. In making the envelope functions and evaluating the overlap integrals numerically, we must make sure that they are properly normalized. Normalization of the wavefunctions is obtained through the following relations

$$F_i\ (\text{norm}) = \frac{F_i}{\sqrt{N_i}} \qquad \text{where} \qquad N_{h,l} = <F_h \mid F_h> + <F_l \mid F_l>,$$

$$N_e = <F_e \mid F_e> . \qquad (4.18)$$

4.2.3. Expression for Gain and Spontaneous Emission

4.2.3.1. Gain

The correct expression for the gain for bulk or QW material can be written in MKS units as [Yan90]

$$g(E) = [(\frac{2\pi}{\hbar})(\frac{e}{m_o})^2(\frac{2\hbar\omega/\varepsilon V}{4\omega^2})\,|M_T|^2\,\rho_{rd}(E)\,] \qquad (4.19)$$

$$.[\frac{n}{c}]\,[f_c(1-f_v) - f_v(1-f_c)]$$

$$= (\frac{2e^2\,\hbar}{\varepsilon_o n c m_o{}^2 E})\,|M_T|^2\,\rho_{rd}(E)\,(f_c - f_v) \qquad (4.20)$$

The first term in (4.19) is an expression for Fermi's Golden Rule which expresses the probability per unit time for transitions occuring from a filled state to an empty state. The second term converts the probability per unit time into probability per unit length. The third term represents the probability that the initial state is filled and the final state is empty. $|M_T|^2$ is the transition matrix element in QW and $\rho_{rd}(E)$ is the reduced density of states, which is given by [Made78]

$$\rho_{rd}(E) = \left[\frac{\rho(k_t)}{dE_{eh}/\,dk_t}\right]_{Eeh=h\omega} \qquad (4.21)$$

where $\rho(k_t)$ is density of states and E_{eh} is the transition energy. For the parabolic energy band, we can get the closed form of reduced density of states. For the nonparabolic bands as in the valence band of quantum wells, ρ_{rd} cannot be given in closed-form. The electron and hole occupation probability, which is determined from the Fermi-Dirac distribution for electrons in the conduction and valence bands, is defined as

$$f_{c,v} = \frac{1}{1 + \exp\left[(E_{e,h} - E_{fc,fv})/k_B T\right]}, \qquad (4.22)$$

where $E_{fc,fv}$ are the non-equilibrium quasi-Fermi levels in the conduction and valence bands. For the parabolic energy band, transition energy can be written as

$$E_{eh} = E_e - E_h = E_g' + \frac{\hbar^2 k^2}{2m_c} + \frac{\hbar^2 k^2}{2m_v}, \qquad (4.23)$$

and the individual energies $E_{e,h}$ are related to the transition energy, E_{eh}, by

$$E_e = E_c + (E_{eh} - E_g')\frac{m_r}{m_c}, \; E_h = E_v - (E_{eh} - E_g')\frac{m_r}{m_v} \qquad (4.24)$$

The primed band gap energy, $E_g' = E_c - E_v$, is defined as the band gap between two given subbands in a QW and is just the material band edge in bulk material. The reduced mass, m_r, is given by

$$\frac{1}{m_r} = \frac{1}{m_c} + \frac{1}{m_v} \qquad (4.25)$$

4.2.3.2. Spontaneous Emission

The expression for the spontaneous emission rate is useful in calculating the current required to provide a given gain found in (4.20). For the case of k-selection, one must find the radiative component of the current density by evaluating the spontaneous emission rate integrated over all energies. The spontaneous emission rate per unit energy at a given energy ($r_{sp}(E)$ has units of per unit time per unit volume per unit energy) is given by [Yan90]

$$r_{sp}(E) = \left(\frac{2\pi}{\hbar}\right)\left(\frac{e}{m_o}\right)^2\left(\frac{2\,\hbar\omega/\varepsilon}{4\omega^2}\right)|M_{ave}|^2\,\rho_{rd}(E)$$

$$.D(E).\ f_c(1 - f_v) \tag{4.26}$$

where D(E) is the optical mode density, in the material with a refractive index of n, given by

$$D(E) = \frac{n^3E^2}{\pi^2\hbar^3\,c^3} \tag{4.27}$$

, and $|M_{ave}|^2$ is the average momentum matrix element, defined by [Zory92]

$$|M_{ave}|^2 \equiv \frac{1}{3}\sum_{\substack{\text{all three}\\ \text{polarization}}} |M_T|^2 . \tag{4.28}$$

In QW structures, the matrix element is enhanced for certain electric field polarizations and reduced for others [Yama84]. For total spontaneous emission we are interested in the total output of light, not which polarizations of light are being emitted spontaneously. Thus, we take the average strength of the transition matrix element over all three polarization. The integrated spontaneous emission output is just equal to the total radiative recombination of carriers and is therefore equal to the radiative component of the current density required to achieve a quasi-Fermi level separation. The relation can be written as

$$J_{rad} = ed \int r_{sp}(E)\ dE \tag{4.29}$$

where d is the QW thickness.

4.2.3.3. Carrier density and Quasi-Fermi level

The carrier density in a given band can be found for a given quasi-Fermi level by integrating the density of states multiplied by the occupation probability over the entire band. For the parabolic subbands, such as in the conduction band of a QW, we can write the electron concentration as

$$N = \frac{m_c k_B T}{\pi \hbar^2\ d} \sum_n \ln \{ 1 + \exp[-(E_c - E_{fc})/k_B T]\} \tag{4.30}$$

The sum is over all quantized subbands within the conduction band of the quantum well, and the E_c are the quantized energy levels.

For non-parabolic bands, such as in the valence band of a QW, where subband structures are nonparabolic, Eq.(4.30) is no longer valid because density of states becomes a complicated function. In this case, it is more appropriate to find the carrier density by numerically integrating over k-space, because k states are always uniformly distributed in k-space, independent of how complicated the energy bands become. For this case, we have [Zory92]

$$P = 2 \sum_{n} \int_{0}^{k_{max}} \rho(k_t)\,[1 - f_v(E_v(k_t))]\,dk_t \qquad (4.31)$$

where $\rho(k_t) = \frac{k_t}{2\pi d}$ is density of states. The sum is again over all quantized subbands, $E_v(k_t)$, within the valence band of the QW, including both heavy and light hole bands. k_t is the k vector component in the plane of the well and k_{max} represents some numerical limit beyond which the contribution to the integral can be neglected.

4.3. Numerical procedures and results

The multiband effective mass equations were solved numerically using the finite-difference method. This method is very convenient in that an arbitrary QW geometry or potential profile can be handled easily, but the drawback is that the size of the matrix becomes larger for numerical accuracy. After discretizing the differential equations and evaluating the coefficients in (4.14a), (4.14b), and (4.15) for each k_t, the problem reduces to an eigenvalue problem to be solved for the subband energies and the the envelope wavefunction. The material parameters to be used in the calculations are given in Table III. Most bulk parameters were taken from reference [Land82], with the exception of the AlGaAs bandgap which was taken from Casey and Panish [Case78]. The conduction band offset in the GaAs/AlGaAs system was assumed to be 62%, taken from Watanabe [Wata85]. For the Luttinger parameters of GaAs we used the value of $\gamma_1 = 6.85$, $\gamma_2 = 2.1$, $\gamma_3 = 2.9$. The effective masses of electrons and holes in the barrier material were assumed to be the same as those in the QW because of the conversion problem. The difference on the Luttinger parameters and electron effective masses in QW and GRIN regions may introduce small corrections to the wavefunctions and to the subband energy levels of the order of a few meV, which can be neglected as compared with the band-gap energy [Sand87]. Boundary value ($z = \pm$ 46.875 nm) should be chosen such that node point could be matched at GRIN/QW interface to make the potential barrier change smooth and eigenfunction go to zero at boundary. At GRIN/QW interface we used averaged potential value of the GRIN/QW interface. Step size(=dz) was also critical for the numerical conversion and accuracy. In our calculation, matrix size was 400 x 400 and dz was 0.46875 nm.

The E-k dispersion curves for the conduction and valence subbands of 7.5 nm GRIN-SCH-SQW calculated by the k.p techniques are given in Fig. 4-3 and 4-4 respectively. The valence subbands calculated by the k.p method are totally nonparabolic due to the effect of the band mixing which is taken into account in this method. At $k_t=0$, heavy and light holes are exactly decoupled. For a nonzero k_t the increasing admixture of heavy- and light hole states gives rise to strong nonparabolicities in the valence band structure. Some of the bands are seen to have negative zone center effective masses. Subbands are labelled as heavy-hole or light-hole (Fig. 4-5) according to their envelope wave function shape at band edge where in-plane wavector k_t is equal to zero.

Table. III

$Al_xGa_{1-x}As$ bulk parameters

E_g (eV) = 1.424 + 1.247x x < 0.45

E_g (eV) = 1.424 + 1.247x +1.147(x-0.45)^2 x > 0.45

m_c = 0.067 + 0.083x

γ_1 = 6.85 (1-x) + 3.45 x

γ_2 = 2.10 (1-x) + 0.68 x

γ_3 = 2.90 (1-x) + 1.29 x

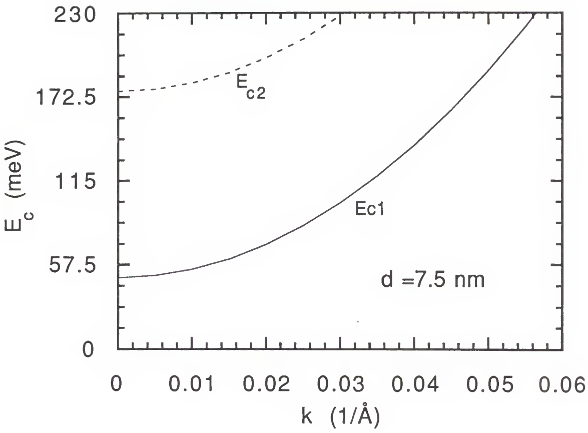

Fig. 4-3. Conduction subband structure of a 7.5 nm GaAs/AlGaAs GRIN-SCH-SQW.

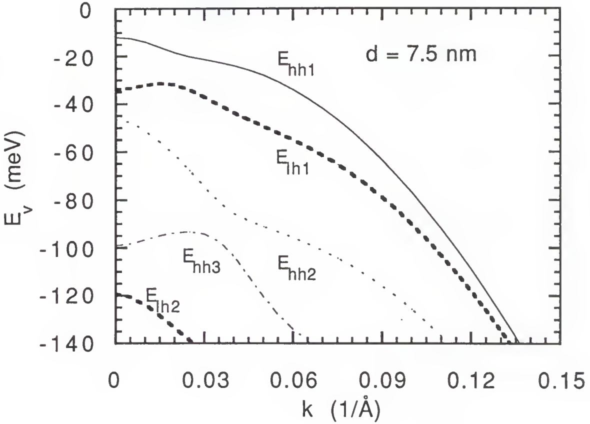

Fig. 4-4. Valence subband structure of a 7.5 nm Ga/AlGaAs GRIN-SCH-SQW.

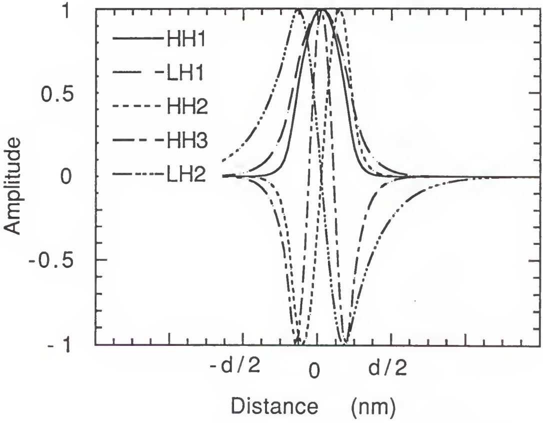

Fig. 4-5. Hole subband envelope wave function at band edge.

In section 4.2.2, we discussed polarization dependent effects in quantum wells. We provided a general method for predicting band edge transition strengths. We can find the TM and TE transition strengths from Eqs.(4.16) and (4.17) for each subband transition as a function of in plane k vector. Figs. 4-6, 4-7, 4-8, and 4-9 show TE and TM transition strength associated with the energy eigenfunctions between conduction and valence subbands. These figures show the selection rules for different polarizations of the optical radiation. Only at $k_t = 0$ is the $\Delta n = 0$ selection rule seen to hold and it is important to note that all of the band-to-band transitions have nonzero matrix elements. The forbidden transitions are allowed in both mode transition due to the redistribution of the transition strength among the various subband transitions. The optical matrix elements are seem to be strongly k_t dependent due to valence band mixing.

The Fermi levels found for a given carrier density, N or P, by assuming charge neutrality, N=P, are shown in Figs. 4-10 and 4-11. Using the Eqs.(4.30) and (4.31), the conduction and valence band quasi-Fermi energy level E_{fc} and E_{fv} with respect to electron (N) and hole carrier density (P) was calculated by integrating the charges within the conduction and valence bands numerically. The density of states can be calculated from the E-k diagrams of Fig. 4-3 and 4-4. The values of the density of states without including spin degeneracy are defined by $\rho(k_t) = \frac{k_t}{2\pi d}$. To simplify the final gain calculation, we used curvefitted equations for the resulting E_{fc} vs N and E_{fv} vs P using polynomial degree of 8. IMSL library PPITT was used for the

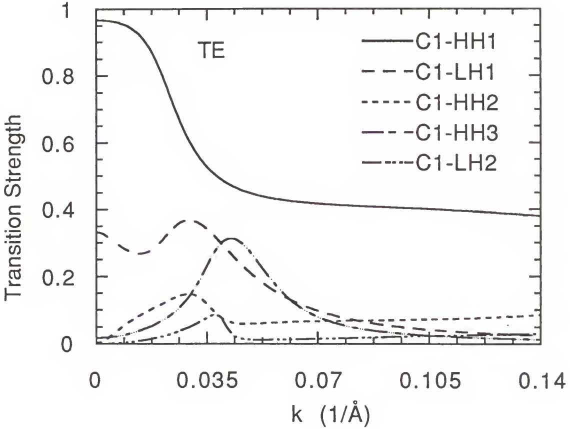

Fig. 4-6. Transition strength for TE light polarization between 1st conduction and hole subbands.

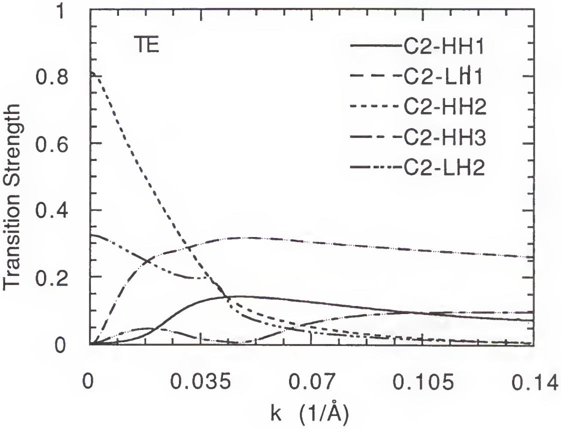

Fig. 4-7. Transition strength for TE light polarization between 2nd conduction and hole subbands.

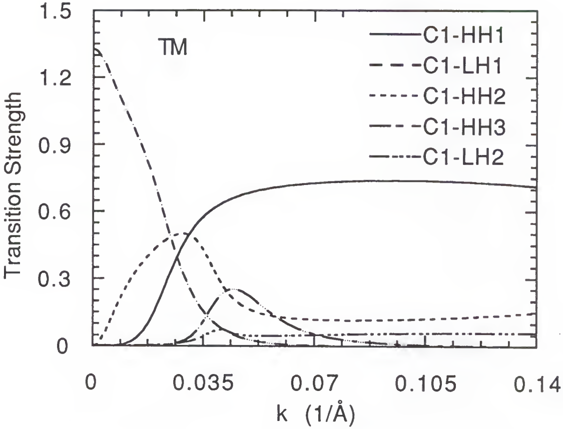

Fig. 4-8. Transition strength for TM light polarization between 1st conduction and hole subbands.

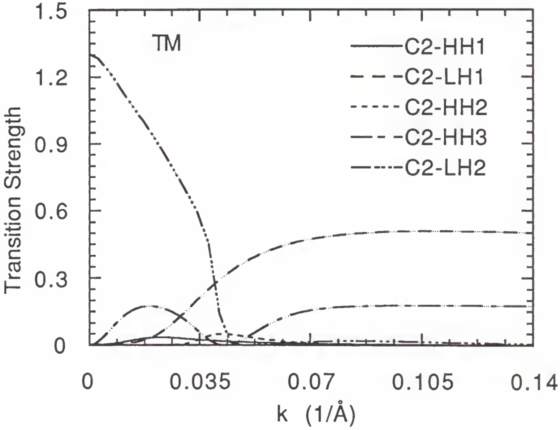

Fig. 4-9. Transition strength for TM light polarization between 2nd conduction and hole subbands.

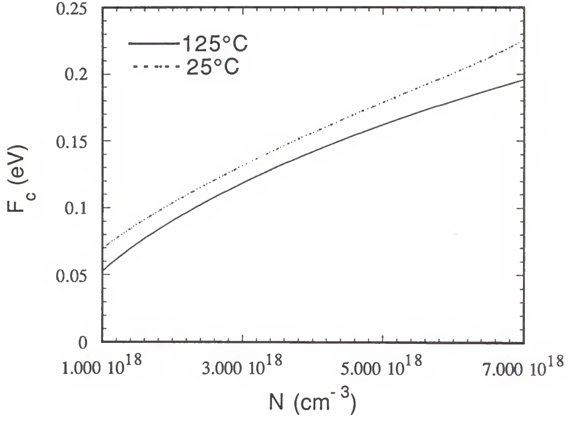

Fig. 4-10. Conduction band quasi-Fermi energy level, Efc vs electron carrier density, N

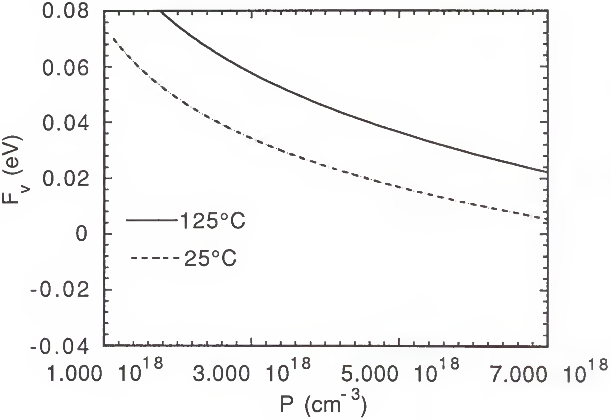

Fig. 4-11. Valence band quasi-Fermi energy level, E_{fv} vs hole carrier density, P

numerical integration of carrier density. However, we could not use the above curve fitted equations for the estimation of reduced density of states because derivative of E with respect to k produced big error. We used cubic spline method (IMSL library PPDER) which gave exact value of reduced density of states.

We then calcaulated the theoretical gain using standard methods [Yan90, Zory92]. Since some of the subbands are double valued in energy, the gain computations are done in the k space. Therefore, the gain is first found between conduction and valence subbands in the k space within the QW plane, and then summed for the transitions having the same energy by using

$$g(E) = \int_0^{\infty} g'(k_t)\, d(E'-E)\, dE' \qquad (4.32)$$

where $g'(k_t)$ is the gain for each k_t increment which is given in Eq.(4.20), and $d(E'-E)$ is the delta function. The g(E) is then the summed gain spectra for each pair of electron and hole subbands. The total gain is then found by simply adding such gain spectra for each pair of subbands (IMSL library PPDER). The results of the TE peak gain as a function of energy are shown in Fig. 4-12 and 4-13 for two different carrier density. These figures show that the forbidden transitions are partially allowed due to band mixing, and the transition shift takes place to n=2 subbands at high carrier density.

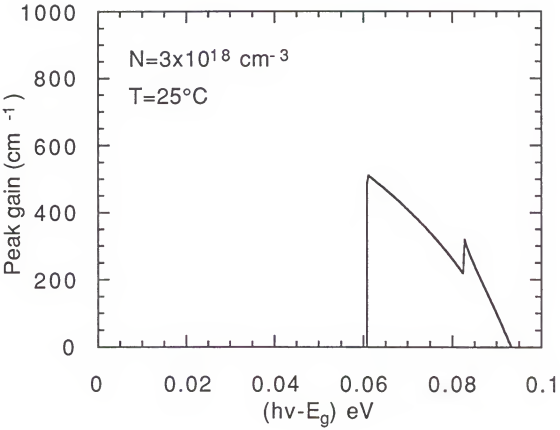

Fig. 4-12. TE mode gain as a function of energy at carrier density $3x10^{18}$ cm^{-3}.

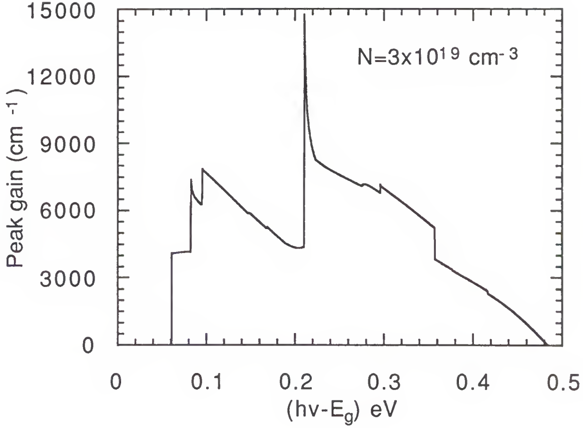

Fig. 4-13. TE mode gain as a function of energy at carrier density 3×10^{19} cm^{-3}.

The results of the peak gain vs J/d calcualation at 25°C for the TE mode are shown in Fig. 4-14 assuming all the injected carriers recombine radiatively ($\eta_{sp}=1$) (black circle: experimental data). For comparison purposes, we have included parabolic band approximation by Chinn. Parabolic model predicts a radiative current density similar to the valence band mixing model for low gain regions. However, valence band mixing model needs more current in high gain region than by the parabolic band model. Fig. 4-15 shows g vs J/d for the parabolic and nonparabolic band strucutre by taking η_{sp} into account. We used measured injection efficiency $\eta_{in}=0.82$ for this calculation [Zmud91]. For Auger recombination rate calculation, we used same formula as in Chinn model [Chin88]. In Fig. 4-16 we compared g vs J/d at 125°C with that of 25°C assuming $\eta_{sp}=1$. Experimental data is for L=500 μm laser and we used α_i value measured at room temperature. We were unable to estimate α_i and η_{in} at this high temperature because η_d vs L measurements were not linear.

4.5. Summary

Combination of the effects by valence band mixing and measured injection efficiency fit the 7.5 nm QW experimental data, leaving no room for the CS contribution. Recent theoretical studies shows that the CS contribution to the threshold current is not as big as reported earlier [Yama81]. It is found that the line shape functions in low dimensional systems have a very small homogeneous broadened widths and strong convergent characteristic [Yama87, Asad89, Ohto91]. Leakage current density estimated in terms of measured injection efficiency (η_{in}) is significant, comparable to the current density contribution by carrier scattering in broadening model.

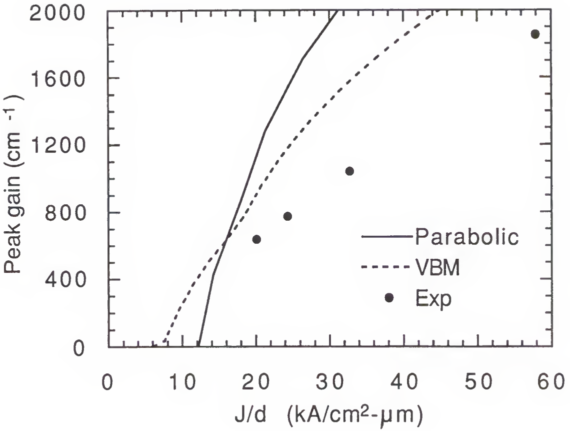

Fig. 4-14. Peak TE mode gain vs J/d assuming all the injected carriers recombine radiatively ($\eta_{sp}=1$) (black circle: experimental data)

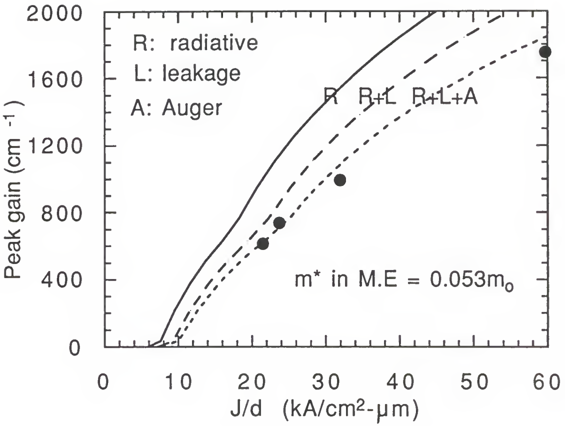

Fig. 4-15. Peak TE gain vs J/d for the parabolic and nonparabolic band strucutre by taking η_{sp} into account.

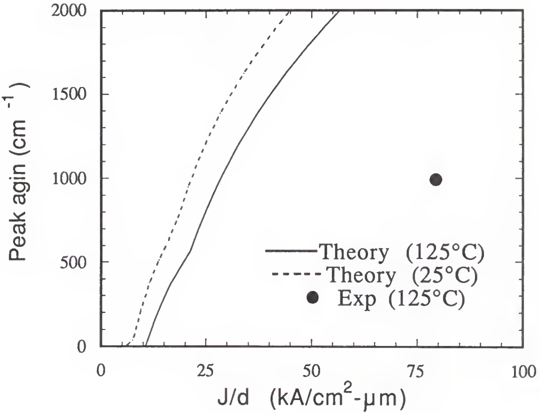

Fig. 4-16. Threshold gain as a function of J/d with η_{sp} = 1 at 125°C.

CHAPTER 5
SUMMARY AND CONCLUSIONS

The goal of this study was to integrate the results of experimental and theoretical work to come up with a model capable of predicting threshold current density (J_{th}) at any temperature for QW lasers. As discussed in Chapter 1, it was necessary to do this since the existing CZR model for QW lasers [Chin88, Chin89] was found to be deficient.

To sort out the problem, we chose two cases, thick 40nm well (bulk) and thin 7.5 nm QW. In thick wells, all the complicated phenomena related to the QW vanish and only CS is expected to be fundamental. We investigated the effect of CS on J_{th} using standard bulk theory. In thin 7.5 nm QW where quantum size and nonradiative effects are important, we studied the effect of CS on J_{th} using new VBM QW theory. The leakage current was included into the total current in terms of spontaneous emission efficiencies (η_{sp}), which can be expressed as the product of two efficiencies, η_{in} = injection efficiency and η_r = active layer radiative efficiency. Injection efficiency was estimated from the differential quantum efficiency versus laser cavity length measurements. Radiative recombination rate was calculated theoretically.

From the above work we found that a reasonable fit to the thick QW(bulk) experimental data at both 25°C and 125°C could be obtained using strict k-selection bulk theory and a knowledge of the carrier injection efficiency(η_{in}). In making the fit, carrier scattering (CS) effect is not necessary, quite contrary to the Yamada's results [Yama81]. The essence of the problem appears to be that if measured J_{th} values are low enough, Stern's theory without CS is sufficient to explain results. This finding suggested the possibility that the effect of CS on J_{th} might not be important even in thin QW lasers. This was verified with VBM QW theory combined with a knowledge of the carrier injection efficiency(η_{in}). Combination of the effects by valence band mixing and measured injection efficiency fit the 7.5 nm QW experimental data, leaving no room for the CS contribution. Leakage current density estimated in terms of measured injection efficiency (η_{in}) is significant, comparable to the current density contribution by CS in the CZR model. This does not necessarily rule out the possibility that experimental spectra can, in principle, be obtained which are subject to the strict k-selection rule. However, recent theoretical studies shows that the CS contribution to the threshold current is not as big as reported earlier [Yama81]. It is found that the line shape functions in low dimensional systems have a very small homogeneous broadened widths and strong convergent characteristic [Yama87, Asad89, Ohto91].

It is concluded that good predictions of threshold current density at any temperature can be made for QW lasers provided one uses QW theory developed in this work and one knows how to predict the temperature dependence of carrier injection efficiency(η_{in}). In our low temperature QW experiments, we were able to determine η_{in} from the differential quantum efficiency (η_d) vs L measurements and get good agreement between theory and temperature. However, we were unable to estimate η_{in} at high temperature because η_d vs L measurements were not linear indicating that η_{in} was a function of cavity length at high temperature. As a consequence, η_{in} at high temperature for the 30/70 QW structures studied here remains to be determined. We are of the opinion that the correct technique for calculating η_{in} has been published recently by Hirayama et al. [Hira92]. It will be interesting to see if the combined theories (the VBM theory developed in this work and that of Harayama et al for η_{in}) are able to make correct predictions of J_{th} for QW structures at any temperature.

REFERENCES

[Abra72] M. Abramowitz and I.A. Stegun, Eds., Handbook of Mathematical Functions, National Bureau of Standards Applied Mathematics Series 55, US. Department of Commerce, Washington,D.C., 1972, Sec.10.4.

[Ahn88] D. Ahn and S.L. Chuang, IEEE J. Quantum Electron., vol.24, pp. 2400, 1988

[Ahn90] D. Ahn and S.L. Chuang, IEEE J. Quantum Electron., vol.26, p.13, 1990

[Alta85] M. Altarelli, U. Ekenberg, and A. Fasolino, Phys. Rev. B32, pp. 5138, 1985

[Anse81] A. Anselm, Introduction to Semiconductor Theory, Mir Publishers, Moscow, 1981

[Asad89] M. Asada, IEEE J. Quantum Electron., vol.26, pp.2019, 1989

[Asada84] M. Asada, A. Kameyama, and Y. Suematsu, IEEE J. Quantum Electron., vol.20, pp.745, 1984

[Ashc76] N.W. Ashcroft and N.D. Merman, Solid State Physics, Holt Rinehart and Winston, 1976

[Bote84] B. Botez, RCA Review, vol.45, pp. 23-32, 1984

[Broi85] D.A. Broido and L.J. Sham, Phys. Rev. B31, pp.888, 1985

[Brum86] J.A. Brum, T. Weil, J. Nagle, and B. Binter, Phys. Rev. B, vol.34, pp. 2381-2384, 1986

[Case78] H.C. Casey and M.B. Panish, Heterostructure Lasers. Academic Press, New York, 1978

[Chan85] Y.C. Chang, Appl. Phys. Lett., vol.46, pp.710, 1985

[Chin84] S.R. Chinn, Applied Optics, vol.23, pp.3508-3509, 1984

[Chin88] S.R. Chinn, P.S. Zory, and A.R. Reisinger, IEEE J. Quantum Electron., vol.24, pp.2191-2214, 1988

[Chin89] S.R. Chinn, P.S. Zory, and A.R. Reisinger, SPIE vol.1043, pp.157, 1987

[Cola87] S. Colak, R. Eppenga, and M.F.H. Schuurmans, IEEE J. Quantum Electron., vol.23, pp.960, 1987

[Corz90] S.W. Corzine, R.H. Yan, and L.A. Coldren, Appl. Phys. Lett. vol.57, pp.2835-2837, 1990

[Dapk82] P.D. Dapkus, Ann. Rev. Mater.Sci.12, pp.243-269, 1982

[Dutt81] N.K. Dutta, J. Appl. Phys., vol.52, pp. 70-73, 1981

[Faso84] A. Fasolino and M. Altarelli, in Two Dimensional Systems, Heterostructures and Superlattices, Springer Verlag, New York, pp.176, 1984

[Garb87] D.Z. Garbuzov, A.V. Tikunov and V.B. Khalfin, Sov. Phys. Semicond. 21, pp. 662-667, 1987

[Hers84] S.D. Hersee, B. de Cremoux, and J.P. Duchemin, Appl. Phys. Lett, vol.44, pp. 476, 1984

[Hira92] H. Hirayama, Y. Miyake, and M. Asada, IEEE J. Quantum Electron., vol.28, pp.68-74, 1992

[Hiro86] T. Hiroshima and R.Lang, Appl. phys. lett, vol.49, pp. 456, 1986

[Lawa71] P. Lawaetz, Phys. Rev. B4, pp. 3460, 1971

[Leop87] M.M. Leop, A.P. Specht, C.A. Zmudzinski, M.E. Givens, and J.J. Coleman, Appl. Phys. Lett, vol.50, pp. 1403-1405, 1987

[Lim91] G. Lim, Y. Park, C.A. Zmudzinski, P.S. Zory, L.M. Miller, T.L. Cockerill, J.J. Coleman , C.S. Hong and L. Figueroa, SPIE Proc., vol. 1418, pp. 123-131, 1991

[Lutt56] J.M. Luttinger, Phys. Rev., vol.102, pp.1030, 1956

[Lutti55] J.M. Luttinger and W. Kohn, Phys. Rev. vol.97, pp. 869, 1955

[Made78] O. Madelung, Introduction to Solid-State Theory, Springer-Verlag, Berlin, 1978

[Nedo71] S.S. Nedorezov, Soviet Physics: Solid State12, pp. 1814, 1971

[Ohto91] T. Ohtoshi and M. Yamanishi, IEEE J. Quantum Electron., vol.27, pp. 46-53, 1991

[Sand85] G.D. Sanders and Y.C. Chang, Phys. Rev. B.31, pp. 6892, 1985

[Sand87] G.D. Sanders and Y.C Chang, Phys. Rev. B35, pp. 1300, 1987

[Schu85] M.F. Schuurmans and G.W.'t Hooft, Phys. Rev.B, vol.31, pp. 8041, 1985

[Shea87] J.R. Shealy, Appl.Phys.Lett, vol.50, pp. 1634-1636, 1987

[Ster73] F. Stern, IEEE J.Quantum Electron., vol.9, pp. 290-294,1973

[Take85] M. Takeshima, J. Appl. Phys., vol.58, pp. 3846-3850, 1985

[Thom80] G.H.B.Thompson, Physics of Semiconductor Laser Devices, Wiley, pp. 250, 1980

[Tsan81] W. T. Tsang, Appl. Phys. Lett., vol.39, pp. 134-137, 1981

[Wata85] M.O. Watanabe, Y. Yoshida, M. Mashiza, T. Nakanisi, and A. Hojo, J. Appl. Phys., vol.57, pp. 5340, 1985

[Yama81] M. Yamada and H. Ishiguro, Jpn. J. Appl. Phys. vol.20, pp.1279-1288,1981

[Yama85] M. Yamada, S. Ogita, M. Yamagishi, and K. Tabata, IEEE J. Quantum Electron., vol.21, pp. 640, 1985

[Yaman84] M. Yamanishi and I. Suemune, Japan. J. Appl. Phys. vol.23, pp. L35, 1984

[Yaman87] M. Yamanishi and Y.Lee, IEEE J. Quantum Electron., vol.23, pp. 367, 1987

[Yan90] R.H.Y an, S.W. Corzine, L.A. Coldren, and I. Suemune, IEEE J. Quantum Electron., vol.26, pp. 213-216,1990

[Ziel87] E. Zielinska, H. Schweizer, S.Hausser, R.Stuber, M.H. Pilkuhn, and G. Weimann, IEEE J. Quantum Electron., vol.23, pp. 969, 1987

[Zory86a] P.S. Zory, A.R. Reisinger, R.G. Waters, L.J. Mawst, C.A. Zmudzinski, M.A. Emanuel, M.E. Givens, and J.J. Coleman, Appl. Phys. Lett, vol.49, pp.16-18, 1986

[Zory86b] P.S. Zory, A.R. Reisinger, L.J. Mawst, G. Costrini, C.A. Zmudzinski, M.A. Emanuel, M.E. Givens, and J.J. Coleman, Electron. Lett., vol.22, pp.475-476, 1986

[Zory91] P.S. Zory, Semiconductor Diode Lasers, SPIE's Educational Short Course at OE/LASE '91, SC3, 1991

[Zory92] P.S. Zory, Quantum well lasers, Academic Press, New York, 1992 (to be published).

[Zmud91] C.A. Zmudzinski, P.S. Zory, G.G. Lim, L.M. Miller, K.J. Beernink, T.L. Cockerill, J.J. Coleman, C.S. Hong, and L. Figueroa, IEEE Phonoton. Technol. Lett., vol.3, pp.1057, 1991

BIOGRAPHICAL SKETCH

Gabgyu Lim was born in Seoul, Korea, 1954. He received the B.S. degree in electrical engineering from Hankuk Aviation College, Seoul, Korea. From March 1978 to July 1984, he was with the Agency for Defence Development, Seoul, Korea, where he worked on the Airforce and Army projects.

He received the M.S. degree in electrical engineering from the University of Florida in 1986. Since August 1986, he has been pursuing his Ph.D degree in electrical engineering in the photonics. From August 1986 to July 1987, he was involved in writing computer model and analyzing lateral mode instability in index guided GaAlAs/GaAs semiconductor diode lasers due to the nonuniformity in active layer thickness of the LPE growth material. From August 1987 to July 1988, he was a teaching assistant of the senior project laboratory class. From August 1988, he has been developing computer model to predict the threshold current density of the QW diode lasers for his thesis.

I certify that I have read this study and that in my opinion it conforms to acceptable standards of scholarly presentation and is fully adequate, in scope and quality, as a dissertation for the degree of Doctor of Philosophy.

Peter S Zory

Peter S. Zory, Chairman
Professor of Electrical Engineering

I certify that I have read this study and that in my opinion it conforms to acceptable standards of scholarly presentation and is fully adequate, in scope and quality, as a dissertation for the degree of Doctor of Philosophy.

Sheng San Li

Sheng S. Li
Professor of Electrical Engineering

I certify that I have read this study and that in my opinion it conforms to acceptable standards of scholarly presentation and is fully adequate, in scope and quality, as a dissertation for the degree of Doctor of Philosophy.

R Srivastava

Ramakant Srivastava
Professor of Electrical Engineering

I certify that I have read this study and that in my opinion it conforms to acceptable standards of scholarly presentation and is fully adequate, in scope and quality, as a dissertation for the degree of Doctor of Philosophy.

G Bosman

Gijs Bosman
Professor of Electrical Engineering

I certify that I have read this study and that in my opinion it conforms to acceptable standards of scholarly presentation and is fully adequate, in scope and quality, as a dissertation for the degree of Doctor of Philosophy.

Timothy J. Anderson

Timothy J. Anderson
Professor of Chemical Engineering

This dissertation was submitted to the Graduate Faculty of the College of Engineering and to the Graduate School and was accepted as partial fulfillment of the requirements for the degree of Doctor of Philosophy.

May 1992

Winfred M. Philllips
Dean, College of Engineering

Madelyn M. Lockhart
Dean, Graduate School